batteries

MDPI

Review

A Review of 3D Printing Batteries

Maryam Mottaghi [1] and Joshua M. Pearce [2,*]

[1] Department of Mechanical and Materials Engineering, Western University, London, ON N6A 3K7, Canada; mmottagh@uwo.ca
[2] Department of Electrical and Computer Engineering, Ivey Business School, Western University, London, ON N6A 3K7, Canada
* Correspondence: joshua.pearce@uwo.ca

Abstract: To stabilize the Earth's climate, large-scale transition is needed to non-carbon-emitting renewable energy technologies like wind and solar energy. Although these renewable energy sources are now lower-cost than fossil fuels, their inherent intermittency makes them unable to supply a constant load without storage. To address these challenges, rechargeable electric batteries are currently the most promising option; however, their high capital costs limit current deployment velocities. To both reduce the cost as well as improve performance, 3D printing technology has emerged as a promising solution. This literature review provides state-of-the-art enhancements of battery properties with 3D printing, including efficiency, mechanical stability, energy and power density, customizability and sizing, production process efficiency, material conservation, and environmental sustainability as well as the progress in solid-state batteries. The principles, advantages, limitations, and recent advancements associated with the most common types of 3D printing are reviewed focusing on their contributions to the battery field. 3D printing battery components as well as full batteries offer design flexibility, geometric freedom, and material flexibility, reduce pack weight, minimize material waste, increase the range of applications, and have the potential to reduce costs. As 3D printing technologies become more accessible, the prospect of cost-effective production for customized batteries is extremely promising.

Keywords: 3D printing; additive manufacturing; batteries; electricity; energy; energy storage; open source; open-source hardware

check for updates

Citation: Mottaghi, M.; Pearce, J.M. A Review of 3D Printing Batteries. *Batteries* **2024**, *10*, 110. https://doi.org/10.3390/batteries10030110

Academic Editor: Matthieu Dubarry

Received: 13 February 2024
Revised: 12 March 2024
Accepted: 13 March 2024
Published: 18 March 2024

Copyright: © 2024 by the authors. Licensee MDPI, Basel, Switzerland. This article is an open access article distributed under the terms and conditions of the Creative Commons Attribution (CC BY) license (https://creativecommons.org/licenses/by/4.0/).

1. Introduction

Global climate change, caused by greenhouse gas emissions from conventional power generation from coal, natural gas, and oil, contributing 18%, 40%, and 1% to global electricity production in 2022, poses a concern [1]. This increases negative impacts on human health [2–4], reduces agricultural productivity [5], and has economic [6–8] consequences. One approach to eliminating the need for fossil fuel electric generation is to replace it with renewable sources to address these challenges [9]. Among the array of renewable energy (RE) options, wind, and solar energy are among the most important due to their widespread availability and abundance [10]. Although these RE sources contributed approximately 11.88% to global energy production in 2022, predictions indicate they could supply up to 50% of the world's electricity demand by 2050 [11,12]. Nonetheless, the inherent intermittency and variability of wind and solar resources make them unable to supply a constant load without storage [13–19]. To address these challenges, various energy storage solutions have been explored, with rechargeable electric batteries emerging as a highly promising option [20]. In addition, with the record growth in electric vehicles (EVs), there is a potential for EV charging to add to stability with a high penetration level RE grid [21]. One of the drawbacks of rechargeable electric batteries is their high cost, and a crucial factor influencing battery production costs is the manufacturing process [22]. In this context, 3D printing technology has emerged as a promising solution to address cost concerns

associated with battery production, offering a layer-by-layer approach, which has already been shown to reduce costs for a wide array of products including those used to conduct battery research such as an open-source ball mill [23], open-source bottle roller [24], sample shaker [25], sample stirrer [26], and numerous additional broader applications [27–29]. Utilizing 3D printing in battery fabrication enhances performance, increases design flexibility, reduces pack weight, minimizes material waste, and shortens production time, ultimately leading to cost reductions [30,31]. Recognizing the enormous potential significance of 3D printing in battery production, this paper provides a detailed review of the most promising 3D printing methods employed in this context. First, to provide background, the types and geometries of batteries (See Appendix A.2) will be summarized. Then, the literature review will focus on enhancing battery properties with 3D printing, including efficiency, mechanical stability, energy and power density, customizability and sizing, production process efficiency, material conservation and environmental sustainability, and solid-state batteries (See Appendix A.1). Finally, the principles, advantages, limitations, and recent advancements associated with the most common types of 3D printing (direct ink writing (DIW), fused filament fabrication (FFF), inkjet printing (IJP), and stereolithography (SLA)) will be reviewed, focusing on their contributions to the field of energy storage. This work will be synthesized and discussed, and conclusions will be drawn on the impact of 3D printing on the electric battery technologies able to back up intermittent renewable energy for the future of a sustainable electric system.

2. Background

2.1. Basic Geometries

Conventional production techniques such as coating operations [32] and screen printing [33] have been extensively employed in the industry to fabricate batteries. These methods offer scalability and reliability but often lack flexibility in design and customization. In contrast, the emerging technologies of 3D printing offer design freedom [30], which leads to customization for specific applications [34,35] and the fabrication of novel and complex structures [36] that were not possible to manufacture through conventional methods and improve the overall performance and efficiency of the batteries. Furthermore, while conventional techniques may excel in terms of established processes and large-scale production capabilities [37], 3D printing offers advantages in rapid prototyping [38] and on-demand manufacturing [39,40].

The geometry of battery electrodes plays a key role in determining both battery application and performance [30,41]. The two fundamental figures of merit for batteries are energy density and power density. Increasing the energy density, however, can negatively impact power density. This occurs due to the longer transport distance for ions within the battery structure, ultimately impeding the rate of energy delivery [42]. Consequently, the manipulation of battery geometry can create a balance between power density and energy density. Battery geometries are shaped by their component architecture, including designs such as thin film [43], 3D porous structure [44], and fiber designs [45]. As these component architectures come together, they result in various battery cell configurations such as sandwich, in-plane, concentric tube, and fiber arrangements. Among these, thin film structures and porous frameworks (grids) stand out as the most common and important forms [30].

2.1.1. Thin Film

The thin film structure is one of the most widely recognized configurations that is readily available in the market and can be fabricated through conventional methods [46]. It is made of rectangular electrodes stacked on top of each other; this can improve the performance through surface area [47]. This structure offers a notable advantage through reduced resistance and a shorter Li+ diffusion length, contributing to an increase in power density [48]. In contrast, the energy density within this configuration is comparatively lower than in other structures. This arises from the limited active content that can be

accommodated in a thin film and further modifications are required to enhance the overall energy density [49].

2.1.2. 3D Porous Structure

The porous structure represents an innovative geometry that can be effectively fabricated using techniques such as 3D printing, in contrast to traditional methods, which often struggle to control intricate geometric structures. Creating pores in various scales in the structure and increasing electrode thickness facilitate ion transport within the structure, which is beneficial to balancing energy and power density. An additional advantage of this design lies in its capacity for electrolyte penetration, enhancing the involvement of ions in electrochemical reactions and improving the battery performance [50–59].

2.2. Impact of 3D Printing on Battery Performance

The advantages that 3D printing provides for battery fabrication include the ability to achieve high-resolution designs [60], ensuring mechanical stability [61], optimizing energy density and power density [61], customizing battery structures for specific applications [62], accommodating a wide range of battery sizes [63], having the fabrication processes with fewer steps and shorter production times [61], enabling rapid fabrication [64], the ability to create all-solid-state batteries [65], and the ability to fabricate and prototype the batteries with novel materials [60]. Moreover, 3D printing in the context of batteries minimizes material wastage, which is beneficial for environmental sustainability [66].

- High resolution and mechanical stability: The advent of 3D printing technology has revolutionized the precision and resolution of battery designs, which directly affects the energy and power density and the overall battery performance [38,67–73]. Furthermore, the ability to fabricate high-resolution geometries through 3D printing results in enhanced mechanical stability [71]. Engineering designs at the microscopic scale make it possible to control the battery structure precisely, ensuring enhanced mechanical performance. Battery properties, particularly during electrochemical reactions when components undergo changes that can impact structural integrity, benefit from mechanical stability [74]. With 3D printing advantages of high resolution, the risk of electrode breakage and battery failure due to structural instability is eliminated, increasing the overall reliability of the battery [75].
- Energy density and power density: 3D printing with the ability to control the design makes it possible to increase active material loading inside the structure with less volume, which results in higher energy density [76–79]. On the other hand, 3D printing's ability to finely control the geometry of battery components plays a critical role in elevating the energy transfer rate within the structure, ultimately resulting in higher power density [80–82].
- Customizability and size: One of the advantages of 3D printing is the design control, which leads to the customizability of the structure. Furthermore, depending on the method and the device resolution, the size can be controlled and the part can be fabricated in a wide range of scales for the production of miniaturized batteries [34,35].
- Efficient production process: In contrast to the conventional method, which consists of multiple steps including slurry preparation, tape casting, material drying, calendaring, material cutting, assembly, electrolyte filling, and final packaging, 3D printing offers notable efficiency. In the 3D printing process, the steps include material preparation, part geometry design, 3D printing, assembly, and optional electrolyte filling, depending on the chosen 3D printing method [83–86]. One of the advantages of 3D printing in battery production is the potential reduction in fabrication time, which is attributed to the straightforward process with fewer steps. Nevertheless, it is crucial to note that the overall fabrication time depends on the specific method employed and any post-treatment requirements [31].

- Minimized material wastage and environmental sustainability: The computer-driven design and fabrication of batteries using 3D printing minimizes material wastage [87], thus lowering production costs [88] and promoting environmental sustainability [30].
- Ability to fabricate all-solid-state batteries: Solid-state batteries, utilizing solid electrolytes instead of liquid counterparts, offer high dimensional integrity, excellent mechanical properties, and enhanced safety [89]. 3D printing, with its precision and design control, facilitates the engineering and fabrication of solid-state electrolytes compatible with electrode configurations, which results in all-solid-state batteries through which all the components can be printed on top of each other. This approach eliminates the need for glove boxes, making production more cost-efficient and environmentally friendly [90–93].
- Ability to fabricate batteries with novel materials: One of the key advantages of 3D printing is its ability to fabricate battery components using novel materials [94]. For instance, the performance of the metal–organic frameworks (MOFs) with carboxyl functionalized channels, which have been proven as extraordinary bi-functional materials usable in both lithium and zinc batteries [95], can be improved further using 3D printing by controlling the design and structure (e.g., 3D printing provides geometric design freedom) [96]. This unique ability enables researchers to explore cutting-edge materials in battery architectures with high precision which not only facilitates rapid prototyping but also opens up possibilities for developing next-generation energy storage solutions that take advantage of the innovative materials [60].

2.3. Goals of Geometric Design for Batteries

Specific designs in batteries can solve many scientific or engineering issues and provide the battery with the opportunity to improve the overall performance in specific applications. The main purpose of controlling the design of batteries is to improve the most important properties, including energy density, power density, cycle life, and safety.

- Energy density and power density: The design helps the user to fabricate the battery component based on the mechanical configuration of the device which makes it possible to customize the shape and size of the battery. With design freedom, batteries can be fabricated with complicated integration and controlled distance between the components to receive the best properties of the battery. The 3D-printed electrodes facilitate ion transfer, which results in high energy density and high power density [30,97,98].
- Cycle life and safety: The arrangement of electrodes and the distribution of active materials impact uniform charge and discharge cycles, thus affecting cycle life [99]. Additionally, the geometry can improve thermal management, preventing overheating and enhancing safety [100]. Moreover, proper separator and electrolyte design, as well as internal pressure management mechanisms, contribute to safety and longevity [78,101].

3. Review

In recent years, 3D printing technology has emerged as a groundbreaking approach for the fabrication of batteries, offering advantages in terms of design flexibility, customization, and rapid prototyping. Various 3D printing methods with their unique characteristics and potential applications have been explored for battery manufacturing. This literature review aims to introduce four of the most promising 3D printing methods for battery fabrication: direct ink writing (DIW), fused filament fabrication (FFF), inkjet printing (IJP), and stereolithography (SLA) (Figure 1). First, the principles, advantages, and limitations will be examined and then recent advancements associated with these techniques will be discussed, revealing their contributions to the field of energy storage.

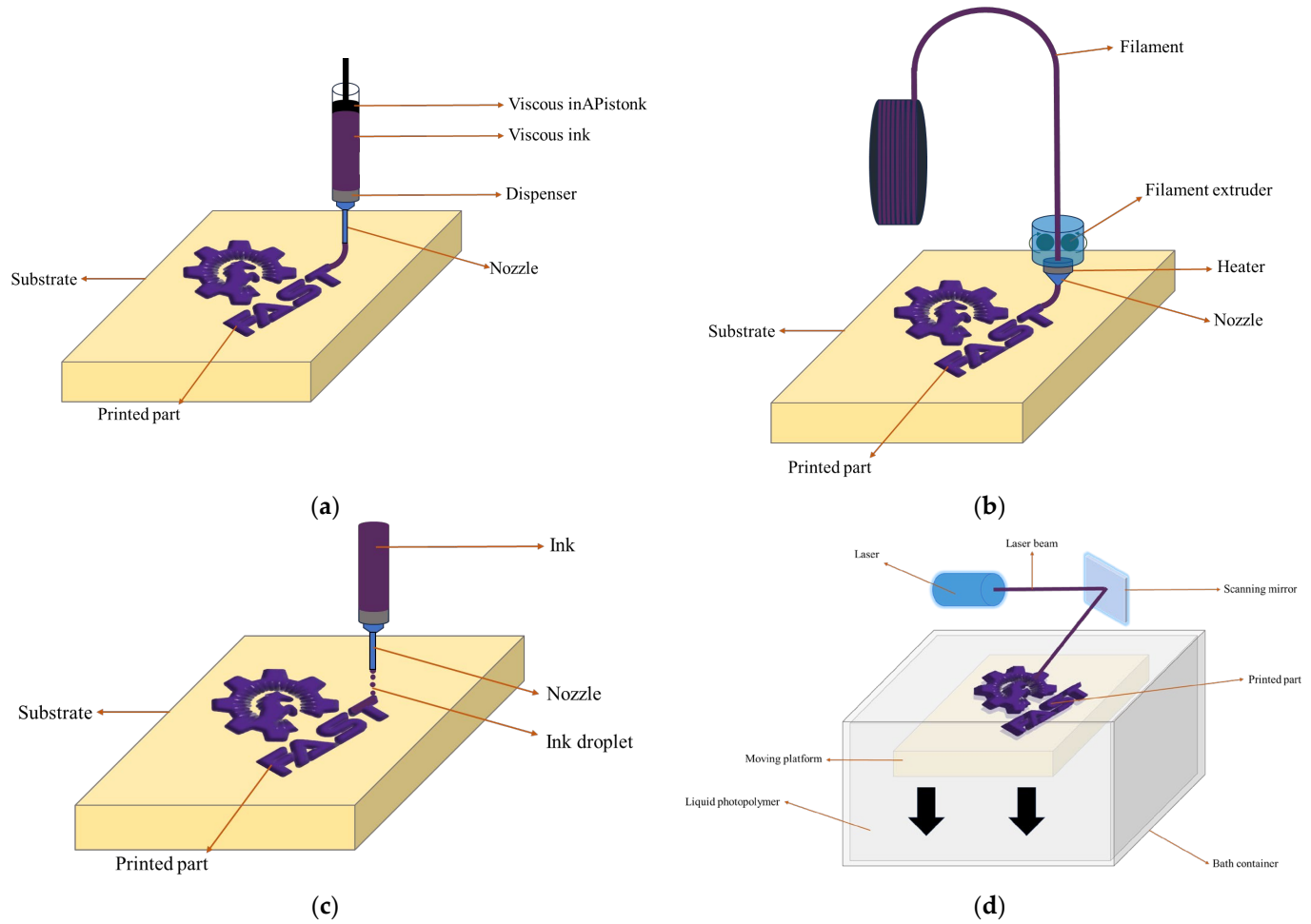

Figure 1. Illustrations of (**a**) DIW, (**b**) FFF, (**c**) IJP, and (**d**) SLA.

3.1. Direct Ink Writing

DIW is a 3D printing technique employed in battery fabrication, relying on the precise extrusion of inks or pastes through a nozzle to create an integrated three-dimensional structure. In DIW for battery manufacturing, the ink typically comprises active materials, conductive materials, binders, and solvents. The extrusion process is characterized by high controllability governed by parameters such as pressure, speed, and nozzle size, allowing for the precise positioning of materials [102–104].

One of its features is the resolution it offers over the creation of complex structures and well-aligned lattice designs, which are advantageous for achieving high porosity and facilitating ion transport in energy storage devices with the least material wastage. The resolution of 3D structures printed using DIW is determined by factors such as nozzle diameter, applied pressure, and ink characteristics, typically ranging from 1 to 250 µm [102,104–106]. Furthermore, compared to other 3D printing methods, DIW can be a more affordable choice, making it accessible to a broader range of applications. Moreover, this method is known for its ease of fabrication and typically requires minimal or no post-production treatment [107]. Another key advantage of DIW is the flexibility in material selection, allowing for the use of a wide range of printing feedstocks including metals, ceramics, polymers, and composites, which empowers the users to select materials that align with the specific applications [104,108]. Moreover, this method has the advantage of printing multi-material structures through the use of multi-nozzle printers or by employing a print–pause–print strategy and swapping syringes containing different materials [109–113].

One of the challenges of DIW is the need for specific techniques to prepare desirable ink formulations. The ink must exhibit viscoelastic and shear-thinning properties to resist gravity-induced deformation and capillary forces during the printing process. The selection of materials and their rheological properties directly influence the quality of the final printed components, contributing to the time-consuming nature of the method [114]. Another limitation lies in the mechanical properties of DIW-fabricated structures. While DIW has precision and customization, the resulting printed components may exhibit poor mechanical properties compared to conventionally manufactured batteries [115].

Some examples of DIW of batteries include:

The study by Ye et al. focused on the multi-layer biscuit structure feature in the development of a 3D graphite at graphite/silicon oxide (Gt@GS) electrode with high loading using direct ink writing technology. They achieved a remarkable reversible capacity of 3.52 mAh cm^{-2} at 3.6 mA cm^{-2} after 120 cycles. Comparisons between Gt@GS and GS electrodes revealed improved cycling performance and reversible capacity for Gt@GS, with a discharge capacity of 9.28 mAh cm^{-2} after 50 cycles. Cycling performance analysis further demonstrated remarkable reversible capacities for Gt@GS even after 120 cycles, attributed to the dampening effect of Gt layers on Si volume expansion. EIS analysis of 3D Gt@GS electrodes indicated reduced charge transfer resistance, which indicates enhanced ion diffusion facilitated by the 3D structure. Additionally, optical microscopy results highlighted significant thickness changes and cracks in grids of 3D GS electrodes after the first discharge, whereas 3D Gt@GS electrodes exhibited minimal thickness changes and deformation [116].

Li et al. used the advantages of DIW to develop a highly conductive reduced graphene oxide (rGO) with Super-P (rGO-P) aerogel composite anode with a high resolution and complex hierarchically porous structure. The optimized rGO-P aerogel electrode demonstrated a superior initial discharge capacity of 848.4 mA h at 80 mA cm^{-2}, a 14.9% improvement over traditional graphite electrodes with 61.8% capacity retention over 100 cycles. Additionally, the coulombic efficiency was higher than 95% over 100 cycles. The rGO structure after 3D printing exhibited integrated macroscale and microscale porous structures with wrinkled sheets, which shows the precise control and design flexibility of the parts made using 3D printing. These structures provide active sites for electrochemical reactions. Furthermore, the rGO-P, with decreased oxygen content, left abundant defect sites that can provide paths for vanadium ion transformation. Moreover, the rGO-P composite has a significantly larger specific surface area which offers ample sites for vanadium ions. Charge–discharge tests showed the superior performance of rGO-P compared to conventional ones, which is attributed to enhanced conductivity, increased reaction sites, and improved mass transfer facilitated by the porous structure [117].

In another study, Zhu et al. fabricated high-resolution metallic 3D Zn electrode structures using DIW. These designs with submillimeter sizes exhibited low electrical resistivity and high mechanical stability. Mechanical testing revealed that the strengths of 3D-printed Zn lattices are comparable to those of Zn foams produced using conventional methods. The results showed that the cell operated over 50 cycles at high discharge rates of 25 mA cm^{-2} and achieved an average specific capacity of 214.85 mAh g^{-1}, which was the highest amount achieved compared to similar electrodes fabricated using other methods. Moreover, capacity retention over 50 cycles was 108% and an average coulombic efficiency of approximately 87% was achieved. Furthermore, with a cumulative capacity of 7.8 Ah cm^{-2} achieved at a high rate of 25 mA cm^{-2}, this 3D Zn anode offers superior performance compared to the conventional Ni–Zn anodes, which validates the practicality of metallic 3D Zn electrode for high-density alkaline cells [118].

Liu et al. developed $Li_{1.3}Al_{0.3}Ti_{1.7}(PO_4)_3$ (LATP) electrolyte for solid-state electrolytes in lithium batteries using DIW with post-heat treatment to enhance ceramic density, completing the formation of the final LATP solid-state electrolyte structures. They shaped these materials into various forms. Microcracks were observed between layers in the 3D-printed parts; this has a positive impact on ionic conductivity. Moreover, the sintering temperatures

influenced the grain size and densification of the samples. In this regard, 1050 °C resulted in a glass state due to lithium volatilization, which affects ionic conductivity. The final parts maintained a high ionic conductivity of 4.24×10^{-4} S cm^{-1}, which is higher than the ones prepared using other methods (2.05×10^{-4} S cm^{-1}). Through this process, the solid-state battery exhibited a high discharge capacity of 150 mAh g^{-1} at 0.5 C, along with 84% capacity retention with an average coulombic efficiency of approximately 100% over 100 cycles [119].

Tao et al. employed DIW to fabricate high-capacity 3D-printed $LiNi_{0.8}Mn_{0.1}Co_{0.1}O_2$ (NMC) cathodes. Through 3D printing, a crack-free network of NMC particles embedded in conductive carbon black, which was homogeneously distributed within the electrodes, was created. This alleviates binder migration issues and ensures improved electrochemical kinetics and long-term cyclability in high-loading electrodes. The results also showed the reduction in Warburg diffusion impedance which indicates enhanced Li^+ diffusion that was facilitated by the shortened diffusion pathway. The specific discharge capacities for the 1st and 800th cycles were measured at 178.6 and 107.5 mAh g^{-1}, respectively, showing capacity retention of 60.2% over the entire 800 cycles with an average coulombic efficiency of approximately 99.9% at a current density of 1 C. These results were superior compared to those achieved using conventional methods, which were equal to 162.3 mAh g^{-1} in the 1st cycle and 88.3 mAh g^{-1}, which showed a capacity retention of 54.4%, in the 800th cycle. Notably, the free space in the electrodes that were created through 3D printing has the ability to buffer mechanical stress for long-term cyclability. As the results showed, this innovative approach increased the contact area, shortened diffusion paths, and reduced stress, leading to improvement in battery efficiency compared to conventional full cells [120].

Li et al. used DIW to fabricate a square grid electrode structure for lithium-ion batteries. The ink was prepared by combining $LiFePO_4$ (LFP), multi-walled carbon nanotubes (MWCNTs), and Polyvinylidene fluoride (PVDF) powder, forming a homogenized paste with n-methyl-2-pyrrolidone (NMP) as a solvent. Through 3D printing, a cross-linked network structure, which promoted the efficient transmission of electrons and ions, was formed. This structure also contributed to the uniform formation of the solid electrolyte interface (SEI) film and ensured good contact between the electrode and electrolyte. Conversely, the samples prepared through coating lacked this network structure, which hindered particle connectivity. The electrochemical results demonstrated an initial discharge capacity of 143.2 mA h g^{-1} at 0.5 C, aligning with the theoretical specific capacity of 170 mA h g^{-1}. Moreover, the specific charge and discharge capacities remained stable, remaining at approximately 150 mA h g^{-1} even after 100 cycles at 0.5 C, showing capacity retention of 105%. Furthermore, the coulombic efficiency was around 99.9% over 500 cycles at 5 C [121].

Rasul et al. utilized DIW to embed highly aligned boron nitride (BN) nanosheets into PVdF polymer composite electrolytes (CPEs) with complex structures (Figure 2a). The achieved ionic conductivity was 6.74×10^{-4} S cm^{-1}. The initial charge capacity of the cells prepared with CPE-BN was 156 mAh g^{-1}, which was comparable to the theoretical capacity of 165 mAh g^{-1}. The cell exhibited a consistent discharge capacity of 132 mAh g^{-1} over 130 cycles at a 1 C rate (140 mA g^{-1}) and a capacity retention of 90% after 250 cycles. These results are attributed to enhanced dendritic lithium suppression, which is facilitated by aligned BN nanosheets. Additionally, another advantage of the aligned BN is minimizing hotspot formation, resulting in the thermal safety of the battery. The symmetric redox peaks indicated reversible Li^+ ions intercalation and deintercalation which validated successful Li^+ ion transport through the electrolytes. From a materials perspective, CPE-BN inks were synthesized using 0.5 wt% silane-functionalized BN nanosheets that enhanced mechanical, thermal, and electrochemical properties. The silane coupling agent improved the polymer–BN interface, which led to superior thermal conductivity and optimum ionic conductivity. Furthermore, the chain entanglement and molecular interactions between BN nanosheets and the PVdF matrix improved the mechanical properties of the electrolyte while maintaining ductility [122].

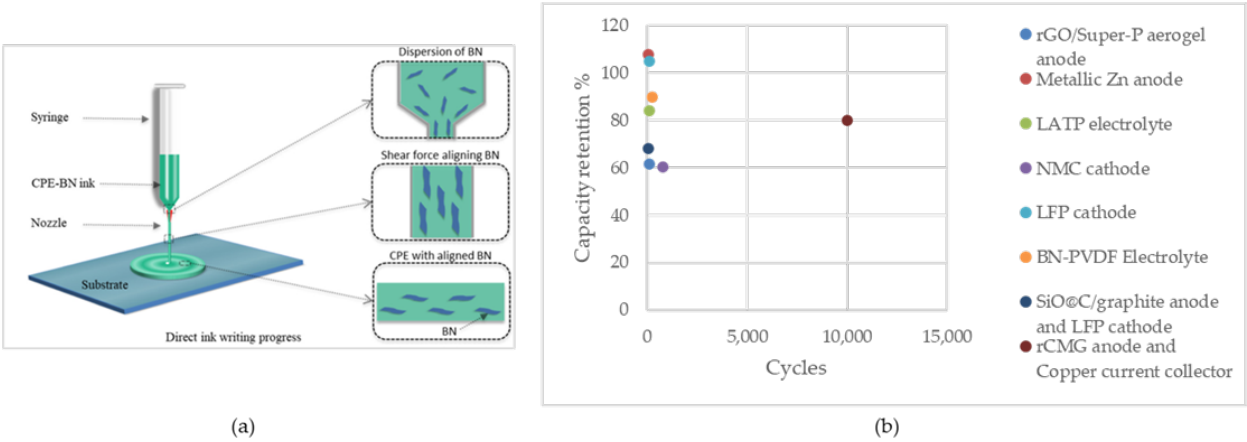

Figure 2. (**a**) Illustration of DIW of aligned BN in electrolyte film. Reprinted/adapted with permission from Ref. [122]; published by ACS, 2022, (**b**) Capacity retention of the cells fabricated using DIW.

Liu et al. utilized DIW for fabricating a comb-like structure of SiO@C/graphite anode and LFP cathode for lithium-ion batteries. The anode ink consisted of SiO/graphite, CNT, and a binder with a weight ratio of 70:20:10 and a solid content of 40% to optimize viscosity. The addition of CNT improved battery efficiency by enhancing the conductive network. Notably, the printed parts exhibited wider line widths and thicknesses than intended due to material expansion during printing. Viscosity analysis revealed shear-thinning behavior, with the 40% solid content ink deemed optimal. The porosity was 60%, facilitating electrolyte infiltration. Results showed that smaller nozzle tips and increased mass loading resulted in higher areal capacity. Additionally, cyclic voltammetry indicated lithium reacting with SiO to form lithium silicate and Li_2O, acting as a volume buffer. The conventional electrodes initially boast a capacity of 517 mAh g^{-1}, whereas the 3D printed counterparts exhibit a slightly lower initial capacity of 485 mAh g^{-1}. SEM analysis suggests that some Si particles within the structure do not actively engage in the reaction; these are referred to as dead Li. Despite exhibiting lower initial capacity compared to conventional electrodes, the 3D printed electrodes demonstrated a capacity retention of 68.2% after 80 cycles, with the initial coulombic efficiency improving from 70% to 100% after the first few cycles [123].

Rocha et al. 3D-printed reduced carbon-modified graphene (rCMG) as a self-standing binder-free anode onto a 3D-printed copper current collector using Pluronic F127 polymer. Pluronic F127, known for its thermoresponsive properties, forms a hydrogel when mixed with water, which facilitates the incorporation of active components. The viscosity of the ink can be controlled by temperature. The results demonstrated that rCMG-Pluronic F127 samples exhibited comparable elastic-brittle behavior and electrical conductivity (90 ± 20 S m^{-1}) to those produced with other rCMG-derived aerogels. Additionally, these samples showed lower total impedance, indicating improved contact between the rCMG electrode and the copper current collector, as well as enhanced electrolyte diffusion and penetration into the electrode pores, which were facilitated by printing both components together. Moreover, the electrochemical results showed that the device retained 80% capacitance after 10,000 cycles at 15 A g^{-1}. They showed the potential of multi-material printing in energy applications, including lithium-ion batteries and supercapacitors [124].

Table 1 provides a summary and comparison of the electrochemical performance achieved through the direct ink writing method for batteries. As evident from the results in Table 1, this technique is versatile, which proves its applicability to enhancing battery efficiency in the fabrication of different battery components, including anode, cathode, and solid electrolytes.

Table 1. Summary and comparison of electrochemical performance of DIW of batteries.

Printed Component	Electrochemical System	Discharge Capacity	Coulombic Efficiency	Cycle Numbers	Application	Reference
Anode: rGO/Super-P aerogel	Anolyte: 1.6 mol L^{-1} V^{3+} + 4 mol L^{-1} H_2SO_4 Catholyte: 1.6 mol L^{-1} VO^{2+} + 4 mol L^{-1} H_2SO_4 Membrane: Nafion 117	848.4 mA h at 80 mA cm^{-2}	More than 95%	100	Vanadium redox flow battery	[117]
Anode: metallic Zn	Cathode: NiOOH Electrolyte (gel): Alkaline polyacrylate Separator: Celgard 5150 (Charlotte, NC, USA)	214.85 mAh g^{-1} at 25 mA cm^{-2}	87%	650	Rechargeable alkaline batteries	[118]
Electrolyte: LATP	Li/3D printed LATP CSSE/Li symmetric cell	150 mAh g^{-1} at 0.5 C	100%	100	All-solid-state lithium batteries	[119]
Cathode: NMC	Counter electrode: Lithium foil Electrolyte: LFP in ethylene carbonate:ethylmethyl carbonate (EC:EMC) (3:7 wt%) (Gen II) Separator: Celgard 2325	107.5 mAh g^{-1} at a current density of 1 C	99.9%	800	Lithium-ion batteries	[120]
Cathode: LFP	Counter electrode: Metal Li Separator: Glass fiber Electrolyte: 1 M LFP dissolved in a mixture of EC and dimethyl carbonate (DMC)	150 mA h g^{-1} at 0.5 C	99.9%	100–500	Lithium-ion batteries	[121]
Electrolyte: BN-PVDF	Cathode: LFP Anode: Li metal	132 mAh g^{-1} at 1 C rate	N/A	130	Lithium-Metal Batteries	[122]
Anode: SiO@C/graphite Cathode: LFP	Electrolyte 1 M LFP dissolved in a mixture of EC and DMC plus a 2% solution of fluoroethylene carbonate (FEC)	75 mAh g^{-1} at 0.3 C	100%	40	Lithium-ion batteries	[123]
Anode: rCMG/Pluronic F127 Current collector: Copper/Pluronic F127	Counter electrode: silver wire Reference electrode: Ag/AgCl (3 M NaCl) Electrolyte: 1-ethyl-3-methylimidazolium bis(trifluoromethylsulfonyl)imide	N/A	N/A	10,000	Lithium-ion batteries, Supercapacitors	[124]

In Table 2, the fundamental materials employed for ink preparation, alongside the viscosity range observed across various shear rates, are shown. As can be seen, a conventional post-printing drying process is necessary to eliminate residual solvents. In some cases, such as [118], additional heat treatments are applied to the printed component for further structural modifications.

Table 2. Key parameters for the DIW process.

Ink Formulation	Printing Parameters	Fabrication Steps	Design	Reference
Active material: GO aerogel, Super-P Crosslinking agent: $CaCl_2$ solution Ink viscosity: 10^7–10^4 Pa·s viscosity at 10^{-1}–10^2 s^{-1} shear rates	Printing height: 1.4 mm Printing speed: 5 mm/s External diameter: 1.79 mm Inner diameter: 1.24 mm	Ink preparation, 3D printing, freeze-drying at −20 °C for 40 h, drying at 60 °C for 12 h	Layer-by-layer serpentine path	[117]
Active material: Zn powder Binder: Poly(methyl methacrylate)-poly(acrylate)-poly(methyl methacrylate) (PMMA-PA-PMMA) pellets Solvent: Tetrahydrofuran (THF) (2-butoxyethanol) and EGBE Ink viscosity: 10^3–10^0 (30% of Zn), 10^4–10^1 (55% of Zn) and 10^5–10^2 (70% of Zn) Pa·s viscosity at 10^{-2}–10^2 s^{-1} shear rates	N/A	Ink preparation, 3D printing, drying at 80 °C for 2 h, annealing at 600 °C for 20 min	Honeycomb structure	[118]

Table 2. *Cont.*

Ink Formulation	Printing Parameters	Fabrication Steps	Design	Reference
Active material: LATP powder Solvent: DI water and IPA Ink viscosity: 5×10^5–5×10^4 Pa·s viscosity at 5–10^2 s^{-1} shear rates	Nozzle inner diameter: ~330 µm Printing layers: 3–6 layers	Ink preparation, 3D printing, freeze-drying for 12 h at −50 °C, sintering from 650 to 1050 °C	Random designs	[119]
Active material: NMC, conductive carbon black Binder: Polyvinylidene fluoride Solvent: NMP Ink viscosity: 5×10^2 Pa·s viscosity at 10^{-1} s^{-1} shear rates	Needle size: 210 µm Printer bed material: aluminum foil Layer height: 20 µm Printing layers: 20 layers Printing temperature: 60 °C	Ink preparation, 3D printing, drying at 100 °C	Layer-by-layer serpentine path	[120]
Active material: LFP, MWCNT Binder: PVDF powder Solvent: NMP	Ink volume: 3 mL Nozzle inner diameter: 330 µm Extrusion pressure: 2.5–5 MPa Printing speed: 400 µm s^{-1} Layer height: 0.15–0.25 mm	Ink preparation, 3D printing, freeze-drying for 12 h	Layer-by-layer serpentine path	[121]
Active material: BN nanosheet, lithium bis(trifluoromethanesulfonyl)imide (LiTFSI), and N-Propyl-N-methylpyrrolidinium bis(trifluoromethanesulfonyl)imide (Pyr13TFSI) Binder: PVDF powder Solvent: NMP Ink viscosity: 10^3–10 Pa·s viscosity at 10^{-1}–10^2 s^{-1} shear rates	Printer bed material: stainless Steel or cathode substrates Ink storage temperature: 120 °C Nozzle pressure: 7 psi Printing speed: 6 mm s^{-1} Printing temperature: 120 °C Ink thickness: ~250 µm Printing temperature: 120 °C	Ink preparation, 3D printing	Disc shapes	[122]
Active material: SiO@C/graphite and MWCNTs Binder: styrene-butadiene rubber (SBR), carboxymethyl cellulose (CMC) Solvent: 1,4 dioxane and deionized water Ink viscosity: 10^7–10^4 Pa·s viscosity at 10^{-1}–10^2 s^{-1} shear rates	Nozzle inner diameter 260~610 µm Printing temperature: below −20 °C	Ink preparation, 3D printing, vacuum freeze-drying for 12 h	Comb-like designs	[123]
Active material ink 1: Copper Active material ink 2: CMG Solvent: pluronic F127 Ink 1 viscosity: 10^3 Pa·s at 10 s^{-1} shear rate Ink 2 viscosity: 10^2 Pa·s at 10 s^{-1} shear rate	N/A	Ink preparation, 3D printing, freeze-drying for 48 h, heat treatment at 900 °C for 1 h	Layer-by-layer serpentine path for battery, One-leg and two-leg components for supercapacitor	[124]

Figure 2b illustrates the capacity retention of these cells. As can be seen, high-capacity retentions, even exceeding 100%, can be achieved through the fabrication of battery components using this method. This is promising for fabricating high-performance battery cells with a long cycle life.

3.2. Fused Filament Fabrication

FFF is a widely adopted 3D printing technique, including in the field of battery manufacturing. It is used widely by various manufacturers and open-source 3D printing communities, representing the broader category of 3D printing technologies utilizing melted filament deposition. On the other hand, fused filament modeling (FDM), trademarked by Stratasys, is a proprietary 3D printing technology using FFF associated only with Stratasys machines [125]. This process operates by melting a thermoplastic filament in a heated nozzle. FFF was radically reduced in price and improved performance due to the open-source self-replicating rapid prototype (RepRap) project and is now the most popular form of 3D printing [126–128]. Within the context of 3D-printed batteries, FFF is employed to produce essential battery components, including electrodes, solid-state electrolytes, and current collectors. For this purpose, FFF offers the capability to integrate conductive materials into the filament, creating conductive pathways within the battery structure [129–132]. FFF is a widely adopted 3D printing technique, including in the field

of battery manufacturing. This process operates by melting a thermoplastic filament in a heated nozzle. One of the advantages of FFF 3D printing is that unlike DIW, which requires specialized inks, it eliminates the need for ink preparation, which simplifies the printing process [35]. Furthermore, its ability to create complex battery designs with a resolution of 50–200 μm is a feature that enables the fabrication of battery components that may be challenging to produce using conventional methods [35,133].

FFF generates minimal waste during the printing process, which is in alignment with sustainable manufacturing practices [133] and is a mature distributed recycling technology [134–137]. Additionally, the accessibility of FFF along with the user-friendly interface and ease of operation make it an economical choice for battery production [129,138]. In addition to the low cost, FFF printers are capable of high production rates suitable for both prototyping and large-scale manufacturing of battery components [139]. Furthermore, FFF is capable of multi-material printing, which enables its ability to print various battery components on top of each other [140,141].

Despite the advantages, the FFF of batteries presents its own drawbacks. One of the most important challenges of FFF 3D printing is the material selection to formulate a suitable filament which often leads to difficulties in filament fabrication [30]. The integration of active and conductive particles, necessary to enhance electrochemical performance, can diminish the overall printability of the filament, making the production process more complex [142]. Moreover, this incorporation can increase the viscosity of the filament which results in the risk of nozzle clogging during the printing operation [129,143]. Beyond these material-related issues, the printed part has weak mechanical properties in the z-direction due to challenges in ensuring proper layer adhesion [31,88,144] and the inherent anisotropy of the process [145]. Furthermore, the printing process can result in components with lower surface quality [31,146].

Some examples of FFF of batteries include:

Beydaghi et al. utilized FFF to create 3D-printed Si-based electrodes for Li-ion batteries. They fabricated the PLA filament as the polymeric matrix along with carbon-based conductive additives, and Si nanoparticles. The results showed that the coulombic efficiency progressively increased from 90% in the first cycle to 96% after 10 cycles and then remained stable for up to 350 cycles. On the 350th cycle, the electrode exhibited a specific capacity of 327 mA h g^{-1}, coupled with a capacity retention of 95% at a current density of 20 mA g^{-1}. The cycle stability is due to the flexible structure that preserves mechanical integrity during Si lithiation/de-lithiation. Moreover, carbon-based additive flakes contribute to a conductive porous framework that creates voids that aid electrolyte access and accommodate volumetric expansion during lithiation, and maintain electrical connections during de-lithiation. The resistance results showed that the reduction of the PLA reduces the resistance and enhances electron/ion transport, which emphasizes the importance of optimizing the ratio of the PLA and active/conductive components [147].

Maurel et al. developed a 3D-printable graphite/PLA filament by optimizing the graphite content of the filament along with the plasticizer for lithium-ion battery electrodes. The solvent selection as well as the ratio of the active material, plasticizer, and PLA ensure the homogeneous integration of the composite and provide a balance between mechanical properties and printability. Among compositions, the one with the highest amount of conductive additives had an initial capacity of 93 mAh g^{-1} and reached the highest specific capacity of 200 mAh g^{-1} (215% capacity retention) at a current density of 18.6 mA g^{-1} (C/20) over 6 cycles. These results were comparable with the theoretical capacity of the active materials. Additionally, 3D printing facilitated the fabrication of a 250 μm thick anode with remarkable reversible capacity, which emphasizes the scalability and adaptability of this approach in battery fabrication [133].

In another study, Maurel et al. produced PLA/LFP as the positive electrode and PLA/SiO_2 as the separator for Li-ion batteries (Figure 3a). The results showed that the melting temperature of the PLA is reduced by adding the active material, which affects the printing temperature. Notably, the amount of plasticizer had a positive effect on the solid

load as the results showed that the solid load should not exceed 50 vol% with PEGDME500 as a plasticizer and 30% without the plasticizer. When PLA/Graphite was used as the negative electrode, the results showed that the composition of 10% conductive material had the highest specific capacity of 165 mAh g^{-1} at C/20 over 30 cycles (97% capacity retention), close to the theoretical capacity. Furthermore, the infill pattern in 3D printing was set to 70% to enhance liquid electrode uptake and prevent short circuits caused by lithium dendrite propagation under adverse cycling conditions. Another remarkable finding was that FFF of the entire battery in "one shot" was possible with this technique, which can be further improved by employing a multi-nozzle 3D printing method [148].

Gao et al. improved aqueous rechargeable zinc-ion batteries by designing hierarchical core–shell cathodes by integrating the FDM and atomic layer deposition (ALD). In their work, the FFF-printed porous carbon network provided an electron-conductive core and ion diffusion channels, while V_2O_5 deposited through the ALD served as an active shell. The results showed that the porous structure of carbon frameworks facilitates ion diffusion while the amorphous V_2O_5 offers isotropic diffusion pathways and abundant active sites. The high diffusion coefficient in the electrode was further studied through the galvanostatic intermittent titration technique (GITT), which exhibited high values, indicating facilitated Zn^{2+} diffusion comparable to conventional pairs. These characteristics resulted in enhanced battery performance, with a specific capacity of 425 mAh g^{-1} at 0.3 A g^{-1}, and 233 mAh g^{-1} at 3 A g^{-1} current density. The capacity at 3 A g^{-1} current density reduces to 183 mAh g^{-1} after 200 cycles and 133 mAh g^{-1} after 800 cycles, showing 78.5% and 57.1% capacity retention, respectively. Additionally, the coulombic efficiency was around 99.9%. The results demonstrate that this method enables the fabrication of binder-free and conductive-additive-free electrodes [149].

Foster et al. utilized a graphene/PLA filament with controllable graphene content, ranging from 1 to 40 wt%, with an optimal load of 15–20% that showed sufficient conductivity as well as mechanical stability. These filaments enabled the creation of 3D-printed freestanding anodes with sufficient conductivity and printability, which led to the elimination of the need for a copper current collector. The results showed that the initial specific capacity was 500 mAh g^{-1} and reached about 100 mAh g^{-1}, with a coulombic efficiency of around 99.9% at 40 mA g^{-1} over 200 cycles. Comparing the achieved capacity with the theoretical capacity of graphite (375 mAh g^{-1}) and graphene (744 mAh g^{-1}), it can be concluded that this capacity lies between these two values. It is clear that the 3D-printed anode exhibits graphene-like electrochemical performance. One of the key steps in achieving these results was chemical treatment with NaOH, which improved the amount of porosity in the samples, leading to enhanced electrolyte wetting and improved battery performance [150].

Hu et al. produced TPU-LFP, TPU-LTO (Lithium titanate), TPU-Graphite, and TPU-NCM filaments and printed high-performance cathodes and anodes via FDM (Figure 3c). The easy fabrication of these active filaments, with excellent homogeneity, stability, and mechanical properties, highlights their potential for industrial-scale fabrication for 3D-printed lithium-ion batteries. The cells made with a TPU-LFP cathode had an initial capacity of 114.1 mAh g^{-1} with 99.12% capacity retention (113.1 mAh g^{-1}) and 99.75% coulombic efficiency after 200 cycles, and 98.9% capacity retention after 400 cycles. Moreover, the cell made using the TPU-LTO anode had 117.2% capacity retention increasing from 102.4 to 120.0 mAh g^{-1} with 100.39% coulombic efficiency over 200 cycles, and 97.94% capacity retention with 99.04% coulombic efficiency over 270 cycles. Additionally, the full cell assembled by the TPU-LFP cathode and TPU-LTO anode exhibited 97.1% capacity retention at a rate of 0.3 C and a coulombic efficiency of 97.4% after 50 cycles. The capacity retention in this work is higher compared to similar ones related to the well-integrated mesh structure with pores that facilitate sufficient ionic transport. They also compared the results of the TPU-based electrodes with the PLA-based ones from earlier works, which revealed that the PLA-based electrodes exhibited higher internal resistance and collapsed sooner after cycling due to the weaker mechanical flexibility of this filament, which resulted in irreversible cracks. Consequently, TPU demonstrated more promising results for long-cycling [151].

In another study, Maurel et al. developed a 3D-printable polyethylene oxide/lithium bis(trifluoromethanesulfonyl)imide (PEO/LiTFSI) filament that was designed for use as the electrolyte in lithium-ion batteries. The achieved ionic conductivity was 2.18×10^{-3} S cm−1 at 90 °C, which shows the capability of FFF in fabricating solid-state electrolytes usable at higher temperatures. It is worth mentioning that EIS tests were conducted at three different sample holders: lateral, sandwich, and interdigitated comb. Among them, the lateral sample holder exhibited the highest values of conductivity that can be attributed to polymer chain orientation along the substrate. Furthermore, the reported conductivity in an interdigitated comb holder appeared to be lower compared to the commonly employed sandwich holder. The advantage of the interdigitated comb holder lies in its ability to measure conductivity without requiring precise sample thickness, which minimizes potential measurement errors. Due to the poorer mechanical properties of the PEO/LiTFSI filament compared to the pure PEO ones, some modifications should be made, including lowering the printing temperature, replacing the extruder with an open model for better filament visibility, adding Bondtech drive wheels for smoother filament feeding, removing the heatsink to prevent filament buckling, and installing a larger diameter nozzle for improved printing and good homogeneity in the achieved samples (Figure 3b) [152].

Reyes et al. 3D-printed a hybrid polymer electrolyte using PLA infused with a mixture of EMC, propylene carbonate, and $LiClO_4$. They used 3D-printed LTO along with graphene nanoplatelets as the anode and 3D-printed LMO along with MWCNTs as the cathode. Two sets of experiments were conducted: in the first set, the individual components—electrolyte, anode, and cathode—were printed separately and assembled into a full-cell battery. In the second set, the entire full cell was printed in one shot as a fully-printed battery. These cells were then integrated into wearable electronic devices such as LCD sunglasses and LED bangles. Initially, $LiPF_6$ and $LiClO_4$ were compared as infused salts in PLA. $LiPF_6$ showed a higher ionic conductivity of 1.7 mS cm^{-1} at 20 °C, but it degraded upon exposure to moisture and lost its conductivity. On the other hand, $LiClO_4$ maintained its mechanical integrity and conductivity of 0.085 mS cm^{-1} at 20 °C after exposure to ambient conditions for 24 h. For the electrodes, graphene was chosen for the LTO anode, while MWCNTs were selected for the LMO cathode to create filaments with desired conductivity and high capacity while maintaining printability. In this regard, the larger LMO particles, as active material in the cathode, can provide more electrical contact points with the MWCNT network. On the other hand, the smaller LTO particles interact better with the graphene network. Moreover, the average discharge capacity of the fully assembled cell reached 3.91 mAh cm^{-3} at 20 mA g^{-1}, with an average Coulombic efficiency of over 88.5% after the first 50 cycles. A single-print battery had a lower capacity (1.16 mAh cm^{-3}) compared to fully assembled batteries (3.91 mAh cm^{-3}), possibly due to an incomplete infusion of components. Despite improvements in Coulombic efficiency, the efficiency remained lower than in conventional lithium-ion batteries, possibly due to increased electrical resistivity of the printed electrodes [129].

In their work, Wolf et al. employed indirect 3D printing to fabricate Ti-based electrodes for redox flow batteries with three different ordered unit cells, including the Kenics mixer, the Ross Low-Pressure Drop mixer (RLPD), and the Sulzer mixer (SMX), and compared these designs to disordered 3D porous electrodes. The fabrication process involved 3D printing of a high-impact polystyrene (HIPS) mold, which was then filled with a paste containing 79.4 wt% Ti, 9 wt% epoxy, and 11.6 wt% glycerol. Subsequently, excess materials were removed, and the green body was sintered and finally coated with graphite to make them electrochemically active. Although the disordered structures had a larger surface area, the results from the ordered 3D structures from this work were either similar to or better than the disordered structures. The flow rate results showed that the 3D electrodes in this study minimized local concentration depletion, which enabled higher current densities by providing clear paths and reducing the formation of gaseous by-products. Moreover, ordered 3D electrodes exhibited similar potentials with stable operation for over 10 h. Additionally, at an equal flow rate of 100 mL min^{-1}, the pumping power for structured 3D

electrodes was two orders of magnitude lower than for the disordered electrode, which was attributed to the structured design that creates clear preferential flow paths, reduces pressure losses, and increases mass transport rates [149].

Table 3 provides a summary of examples of FFF-printed battery components, including anode, cathode, separator, and electrolyte, which shows the potential of this method to fabricate all-solid-state batteries.

Table 3. Summary and comparison of electrochemical performance of FFF of batteries.

Printed Component	Electrochemical System	Discharge Capacity	Coulombic Efficiency	Cycle Numbers	Application	Reference
Anode: PLA/Si/graphene	Counter electrode: metallic lithium Electrolyte: 1 M LPF in DC and EC	327 mA h g^{-1} at a current density of 20 mA g^{-1}	96%	350	Lithium-ion battery	[144]
Anode: PLA/Graphite	Counter electrode: metallic lithium Electrolyte: 1 M LPF in DC and EC	200 mAh g^{-1} at a current density of 18.6 mA g^{-1} (C/20)	N/A	5	Lithium-ion battery	[130]
Cathode: PLA/LFP Separator: PLA/SiO_2	Counter electrode: metallic lithium Electrolyte: 1 M LPF in DC and EC	165 mAh g^{-1} at C/20	N/A	~30	Lithium-ion battery	[145]
Cathode: Carbon/V_2O_5	Electrolyte: 2 M $ZnSO_4$ aqueous solution Separator: glass fiber	183 mAh g^{-1} at 3 A g^{-1} current density	99.99%	200	Aqueous zinc-ion batteries	[146]
Anode: PLA/Graphene	Counter electrode: metallic lithium Electrolyte: 1 M LPF in DC and EC	100 mAh g^{-1} at 40 mA g^{-1}	99.9%	200	Lithium-ion battery	[147]
Cathode: TPU-LFP	Electrolyte: 1 M LPF in DC and EC Separator: Celgard 3501	113.1 mAh g^{-1} at a rate of 0.3 C	99.75%	200	Lithium-ion battery	[148]
Anode: TPU-LTO	Electrolyte: 1 M LPF in DC and EC Separator: Celgard 3501	120.0 mAh g^{-1} at a rate of 0.3 C	100.39%	200	Lithium-ion battery	[148]
Anode: PLA/Graphene/LTO Cathode: PLA/MWCNTs/LMO Electrolyte: PLA/PC:EMC:$LiClO_4$	Separator: polypropylene disk	3.91 mAh cm^{-3} for assembled cell and 1.16 mAh cm^{-3} for the single-print cell at 20 mA g^{-1}	88.5%	50	Lithium-ion battery	[126]
Cathode: Ti-based electrode	Anode: zinc plate Separator: Nafion 117 membrane	N/A	N/A	N/A	Redox flow battery	[149]

In Table 4, the key components for filament preparation along with the printing temperature, fabrication steps, and design considerations are outlined. Notably, the printing temperature is determined by the filament composition and typically requires adjustment to be approximately 15 degrees higher than the melting temperature of the filament composite [130]. Furthermore, 3D printing enables the creation of customized shapes, which offers significant benefits for real-world applications.

Table 4. Key parameters for the FFF process.

Filament Formulation	Printing Parameters	Fabrication Steps	Design	Reference
Active material: carbon black, silicon, graphite-based powder Filament substrate: PLA	Filament diameter: 1.75 mm Nozzle diameter: 0.4 mm Nozzle temperature: 210 °C Bed temperature: 60 °C Printing speed: 40 mm s^{-1} Infill density: 100%	Filament preparation using a twin-screw extruder, 3D printing	Circular disc	[144]
Active material: graphite Plasticizer: PC and poly(ethylene glycol) dimethyl ether Solvent: dichloromethane (DCM) Filament substrate: PLA	Z-Direction resolution: 0.25 mm Filament diameter: 1.75 mm Nozzle diameter: 0.4 mm Nozzle temperature: 150 °C Bed temperature: 60 °C	Filament preparation, 3D printing	Circular disc	[130]
Active material filament 1 (negative electrode): graphite Active material filament 2 (positive electrode): LFP Active material filament 3 (Separator): SiO_2 Solvent: dichloromethane (DCM) Filament substrate: PLA	Z-Direction resolution (first layer): 0.20 mm Z-Direction resolution (following layers): 0.05 mm Filament diameter: 1.75 mm Nozzle diameter: 0.4 mm Nozzle temperature: 195 °C Bed temperature: 60 °C	Filament preparation, 3D printing	Random customized shapes	[145]
Filament substrate: commercially available conductive carbon filament	Nozzle temperature: 230 °C Bed temperature: 60 °C	3D printing of carbon filament, oven drying at 50 °C for 6 h, atomic layer deposition of V_2O_5	Circular disc	[146]
Active material: graphene Filament substrate: PLA	Filament diameter: 1.75 mm Nozzle temperature: 190 °C	Filament preparation, 3D printing, chemical pretreatment	Circular disc	[147]
Active material: LFP, conductive additive Ketjen Black (KB) Solvent: dimethylformamide (DMF) Filament substrate: TPU	Layer height: 100 µm Nozzle temperature: 260–350 °C Bed temperature: 50 °C	Filament preparation, 3D printing	Random customized shapes	[148]
Active material: LTO, KB Solvent: dimethylformamide (DMF) Filament substrate: TPU	Nozzle temperature: 260–300 °C Bed temperature: 50 °C	Filament preparation, 3D printing	Random customized shapes	[148]
Active material filament 1: LTO, graphene Active material filament 2: LMO, MWCNTs Active material filament 3: PLA/PC:EMC:$LiClO_4$ Filament substrate: PLA	Layer height: 100 µm Filament diameter: 1.75 mm Nozzle temperature: 210 °C Bed temperature: 50 °C Printing speed: 20–40 mm s^{-1}	Filament preparation, 3D printing	customized designed LCD sunglasses and bangles	[126]
Filament substrate: HIPS	N/A	3D printing of mold, electrode filling, curing at 40 for 3 h, sintering at 1000 °C for 90 min	Kenics mixer unit cell, RLPD, SMX	[149]

Figure 3d illustrates the capacity retention of the FFF-printed cells as a function of cycles. As can be seen, the fabricated cells show high-capacity retention.

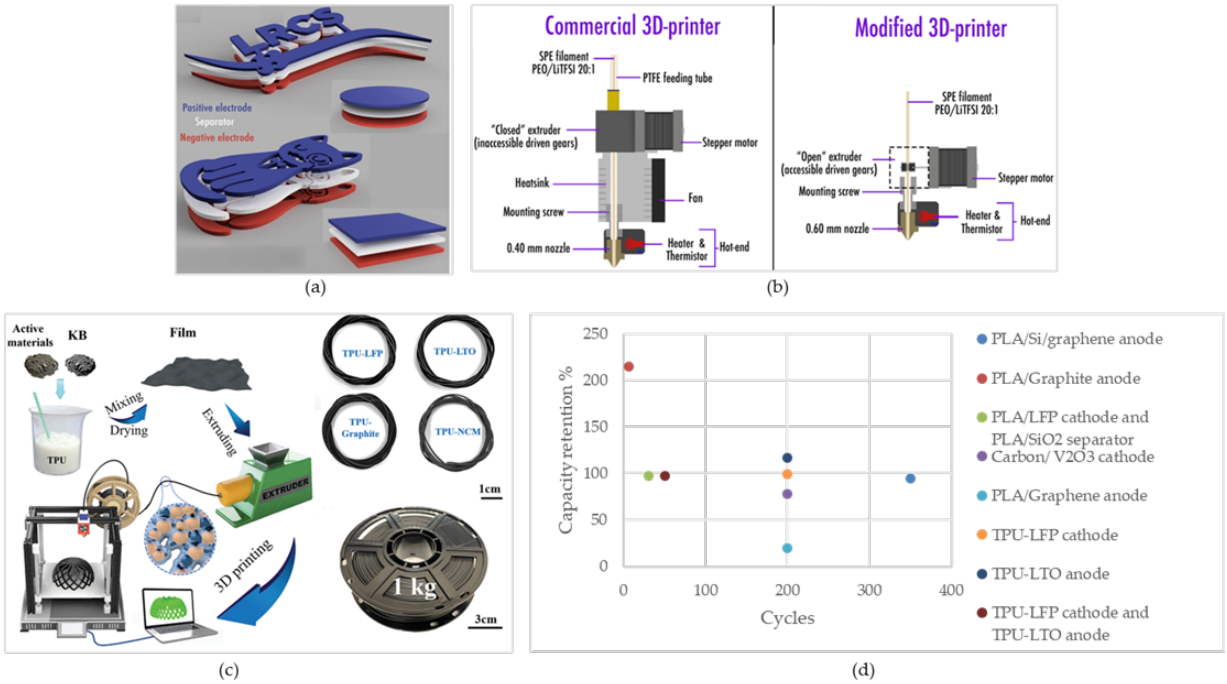

Figure 3. (**a**) "one shot" FFF of battery. Reprinted/adapted with permission from Ref. [145]; published by Scientific Reports, 2019 (**b**) required modifications for printing customized PEO/LiTFSI filament [150], (**c**) illustration of FFF of TPU-based electrodes. Reprinted/adapted with permission from Ref. [148]; published by ACS, 2021, (**d**) capacity retention of the cells fabricated using FFF.

3.3. InkJet Printing

This method operates by selectively depositing small droplets of specialized inks onto a substrate in a layer-by-layer process. The ink contains essential materials for battery components, such as electrodes, electrolytes, and current collectors, finely dispersed within a liquid carrier. After each layer is printed, it may undergo processes like drying or curing before the printer proceeds to deposit the subsequent layer [28,151].

IJP offers numerous advantages in battery fabrication. By depositing precise amounts of the ink only where needed to eliminate waste, IJP ensures that the materials are utilized efficiently, which results in minimizing environmental impact and cost [152,153]. Another advantage is its lower viscosity requirement compared to DIW. This characteristic simplifies the formulation and handling of printable inks, which makes the IJP practical and adaptable for a wide range of materials and applications [151]. This method is also capable of multi-material deposition, which provides controlled deposition of active battery component materials [154]. Moreover, the affordability of IJP equipment along with the ease of use make this technique an accessible choice for the battery manufacturing process [138].

Despite the advantages, a uniform structure printed using IJP can be challenging, and to maintain both battery performance and structural integrity, fine features, and precise adhesion layers are required [151]. Furthermore, while IJP requires lower ink viscosity than DIW, the properties of the ink, such as viscosity and density, need to be optimized to meet the standards. This optimization is essential to avoid issues such as ink agglomeration and nozzle clogging [152].

Overall 3D printing of such batteries has made substantial progress [155]. Some examples of IJP of batteries include:

Lawes et al. utilized IJP for efficient and cost-effective fabrication of silicon anodes using Si nanoparticles and PEDOT:PSS as a conductive binder. Their work demonstrated the significance of selecting a binder for inkjet printing, as it revealed that binders such as PVP and CMC exhibit rapid capacity decay or low initial capacities due to poor reversibility and electron conduction. On the other hand, anodes made using PEDOT:PSS binder

achieved remarkable cycling performance. The SEM results supported this by showing a continuous polymer network maintained during lithiation and de-lithiation that ensures intimate contact with Si nanoparticles. The initial capacity was 3800 mAh g^{-1} in the first cycle and reduced to 2700 in the subsequent cycles. Moreover, the achieved capacity was more than 1700 mAh g^{-1} at 0.1 C, showing a capacity retention of 63% over 100 cycles. The coulombic efficiency starts from 31% and 75% in the first two cycles and increases to 98.6% for the remaining cycles. The electrical conductivity of PEDOT:PSS and reversible deformation properties formed a continuous conductive network, ensuring rapid electron transfer and accommodating SiNP volume changes during charge and discharge [156].

Chen et al. utilized IJP to fabricate a dendrite-free Zn anode with Ag nanoparticles for Zn metal batteries. They inkjet-printed a Ag nanoparticle-modified carbon cloth (AgNPs@CC) that reduces nucleation overpotential compared to bare CC and promotes uniform Zn nucleation. Notably, the increased surface wettability of AgNPs@CC compared to CC indicated improved Zn-ion migration potential of the printed part. Another finding was that AgNPs on CC surfaces ensure uniform electric field distribution, which controls the Zn deposition morphology and reduces dendrite growth and side reactions during cycling. This result highlights the crucial role of AgNPs in modulating Zn nucleation and deposition. Furthermore, AgNPs enhance thermal conductivity, which ensures uniform temperature distribution and suppresses dendrite formation during fast charging and discharging processes. This resulted in an initial discharge capacity of 255 mAh g^{-1} at 5 A g^{-1}, reaching 184 mAh g^{-1} after 1200 cycles with only 0.023% capacity fade rate in each cycle and a coulombic efficiency of about 99.5% within 800 cycles. Nonetheless, as reported in this work, a similar anode fabricated without inkjet-printed Ag nanoparticles exhibited a capacity retention rate of 42.9% after 700 cycles [157].

Kushwaha et al. utilized IJP to deposit graphene inks made from graphene nanosheets in ethanol solvent and ethyl-cellulose stabilizer onto different substrates, including Cu foil. The print was followed by annealing to achieve conductivity and porosity. Based on the Raman spectroscopy results, the samples printed after pyrolysis showed increased ordering, which improves electrical conductivity and lithium-ion storage kinetics. Notably, cyclic voltammetry revealed that lithium intercalation and deintercalation, which is controlled by diffusion, occur at lower potential scan rates, while at higher potentials both Li-intercalation/deintercalation and surface charge storage occur. This indicates significant contributions from both surface and bulk charge storage processes. This phenomenon is attributed to the well-ordered structure of the annealed graphene film. Moreover, SEM and TEM analysis showed a porous structure with interconnected nanoflakes, which also contribute to enhanced electrical conductivity and faster Li-ion insertion and removal. The reversible capacity was about 520 mAh g^{-1} with capacity retention of about 87% after 100 cycles at 2 C, which is a high current density. Furthermore, the initial coulombic efficiency was 95%, reaching more than 99% over 100 cycles. Another important parameter was the dimension of the graphene, which had a thickness of about 3 nm and lateral dimensions of 2–3 nm. These dimensions make the ink suitable for preventing nozzle clogging during printing due to its small size relative to the nozzle diameter [158].

In their other work, Kushwaha et al. used IJP to deposit a graphene layer onto an Al current collector foil, addressing corrosion issues in a cathode current collector. This work significantly suppresses corrosion, which leads to better electrical connectivity. Furthermore, they showed that the number of printing layers with subsequent annealing in an Ar atmosphere at 350 °C was crucial for achieving uniformity and enhancing the electrical conductivity. The results showed about 180 mAh g^{-1} initial capacity at C/5, with ~90% capacity retention. The comparable or superior cyclic stability of the inkjet-printing of graphene on the Al current collector compared to other coating methods offered practical advantages in terms of cost-effectiveness, scalability, and tunability [159].

Viviani et al. investigated the impact of carbon-based additives such as carbon black (CB) and multi-walled carbon nanotubes (CNT) on the electrochemical performance of inkjet-printed thin-film LTO electrodes in lithium-ion batteries. Between the carbon-based

additives, and despite the slightly larger particle dimensions of the CNT, the LTO-CNT electrodes showed an optimal compromise between CNT length and conductivity properties. Notably, its impedance increase upon cycling was less compared to LTO-CB, which suggests a more stable and homogeneous SEI formation. As a result, LTO-CNT electrodes achieved the highest specific capacity, reaching 128 mAh g^{-1} at 0.5 C, and exhibited excellent cycle stability with negligible capacity loss (100% capacity retention) and an average coulombic efficiency of 100% over 100 cycles [160].

Kolchanov et al. utilized inkjet printing to fabricate thin-film Li-ion batteries through the optimization of the $Li_{1.2}Mn_{0.54}Ni_{0.13}Co_{0.13}O_2$ (LMR) cathode. It was found that printing resolution significantly influenced the printing quality and duration, which enabled quality enhancement and process time reduction along with drop spacing optimization. Additionally, adjusting the number of deposited layers improved cathode weight and eliminated local printing imperfections. Moreover, the thickness measurements indicated a decrease in the film growth rate with increased layer deposition that was attributed to void filling and ink spreading. Notably, the ordered layered structure of LMR with minimal intrinsic stress facilitated lithium-ion intercalation and deintercalation. The study demonstrated comparable discharge capacities of 240 mAh g^{-1} between inkjet and conventional methods at a 0.01 C rate with 68.7% capacity retention over 70 cycles. It is worth mentioning that the specific energy values of inkjet-printed active layers were comparable to those of high-energy density lithium cell cathode layers used in smartphones, which suggests their potential suitability for similar applications [161].

These examples are shown in Table 5 and represent the effectiveness of IJP in improving battery performance through the fabrication of different battery components.

Table 5. Summary and comparison of electrochemical performance of IJP of batteries.

Printed Component	Electrochemical System	Discharge Capacity	Coulombic Efficiency	Cycle Numbers	Application	Reference
Anode: Si/PEDOT:PSS	Counter electrode: metallic lithium Electrolyte: 1 M LPF in DEC and EC, and ethyl methyl carbonate (EC:DEC:EMC)	1700 mA h g^{-1} at 0.1 C	98.6%	100	Lithium-ion battery	[156]
Anode: AgNPs@CC	Counter electrode: Zn foil Electrolyte: 1 m $Zn(CF_3SO_3)_2$ aqueous solution Separator: glass fiber	184 mAh g^{-1} at 5 A g^{-1}	99.5%	1200 and 800	Heat-resistant zinc batteries	[157]
Anode: graphene onto Cu foil substrate	Counter electrode: Li metal foil Electrolyte: 1 LPF in EC and EMC Separator: glass microfiber filter paper	520 mAh g^{-1} at 2 C	99%	100	Lithium-ion battery	[158]
Current collector: graphene-coated Al	Cathode: $LiNi_1/3Mn_1/3Co_1/3O_2$ (Li-NMC111)	180 mAh g^{-1} at C/5	N/A	100	Lithium-ion battery	[159]
Anode: LTO	Counter electrode: Li metal foil Electrolyte: 50 µL of 1 M LPF in EC:DEC Separator: Celgard 2400	128 mAh g^{-1} at 0.5 C	100%	100	Lithium-ion battery	[160]
Cathode: LMR	Counter electrode: Li metal foil Electrolyte: 1 M LPF EC/PC/DEC/EMC/PA Separator: Celgard 2325	240 mAh g^{-1} at 0.01 C	N/A	70	Lithium-ion micro batteries	[161]

In Table 6, the foundational materials utilized in IJP are shown. Notably, similar to DIW, a post-printing drying process is essential to remove any residual solvent, ensuring the integrity of the printed structure and reducing the effect of the non-conductive and non-active components, which have negative effects on battery performance. Moreover, the majority of the samples fabricated through IJP are in thin film designs, along with the higher power density in battery performance as mentioned earlier.

Table 6. Key parameters for the IJP process.

Ink Formulation	Printer Parameters	Fabrication Steps	Design	Reference
Active material: SiNPs carbon black Binder: PEDOT:PSS, Polyvynilpirrolidone (PVP), CMC Solvent: DI-water Ink viscosity: 10 mPa·s	Printing temperature: Ambient Number of printed layers: 25	Ink preparation, 3D printing, drying in a vacuum oven at 60 °C overnight	N/A	[156]
Active material: conductive silver Solvent: Triethylene glycol monethyl ether Ink viscosity: 9~11 cPa·s	Printhead diameter: 60 µm Droplet diameter: 45–55 µm	Ink preparation, 3D printing, annealing at 180 °C for 1 h	Layer-by-layer serpentine path	[157]
Active material: graphene nanosheets Binder: ethyl-cellulose Solvent and solution: ethanol and terpineol (anhydrous), NaCl	Printhead diameter: 80 µm Droplet diameter: 90–110 µm Printing speed: 50 mm s^{-1} Printhead temperature: 30 °C Substrate temperature: 60 °C	Ink preparation, 3D printing, annealing at 350 °C for 1 h and 30 min	Thin film	[158]
Active material: graphene nanosheets Binder: ethyl cellulose Solvent: ethanol/terpineol	Droplet volume: 110 pL Droplet step size: 100 µm Printhead temperature: 30 °C Substrate temperature: 60 °C	Ink preparation, 3D printing, annealing at 350 °C for 1 h and 30 min	Thin film	[159]
Active material: $Li_4Ti_5O_{12}$ powder, carbon-based conductive agent (CB por CNT), 1 mM lithium dodecyl sulfate (LDS), lithium polyacrylate (Li-PAA) Binder: PVP Solvent: ethylene glycol (EG), 2-propanol (IPA) Ink viscosity: 2.5–3 cPa·s viscosity at 10–10^4 s^{-1} shear rates	Printhead diameter: ~30 µm Printhead resolution: 600 dpi	Ink preparation, 3D printing, drying at 80 °C for 3 h	Thin film	[160]
Active material: LMR, carbon black Binder: PVDF Solvent: NMP Ink viscosity: 3–20 cPa·s viscosity at 25–34 mN m^{-1} surface tension	Droplet volume: 10 pL Substrate temperature: 45 °C	Ink preparation, 3D printing, oven drying at 200 °C for 2 h	Thin film	[161]

Figure 4 illustrates the capacity retention of the IJP cells. As can be seen, the Ag-NPs@CC anode fabricated using this method shows high capacity retention of 100% over 1200 cycles, which is noticeable and indicates the high electrochemical performance of the cell.

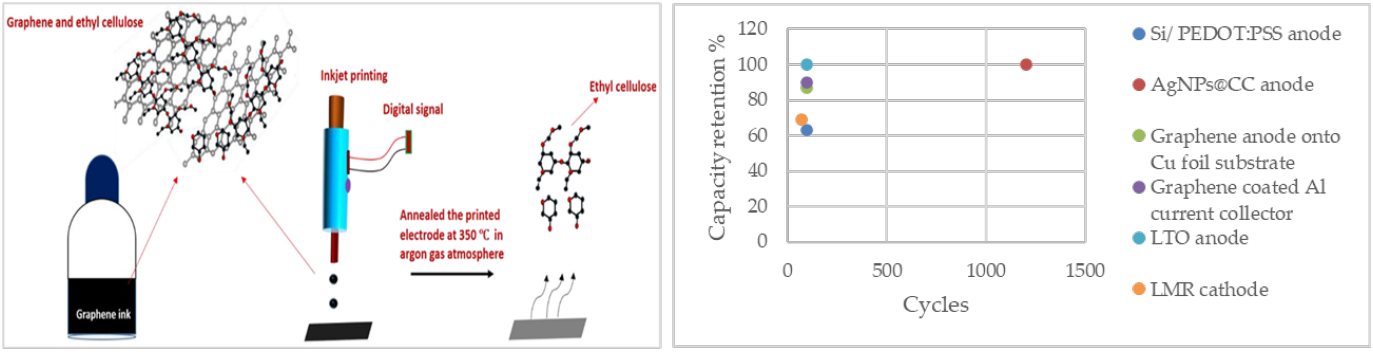

(a) (b)

Figure 4. (**a**) Illustration of the IJP process of fabricating a graphene thin-film electrode. Reprinted/adapted with permission from Ref. [158]; published by ACS, 2022 (**b**) capacity retention of the cells fabricated using IJP.

3.4. Stereolithography

SLA, a prominent light-assisted 3D printing technology, operates by employing a light source to solidify a polymer resin selectively layer by layer. The versatility and precision offered by SLA make it a valuable tool in various industries, with notable applications emerging in energy storage systems [28,162,163].

One of the advantages of SLA is its high resolution, which can reach up to 0.5 µm, making it well-suited for applications demanding complex geometries [27,70,164,165]. Additionally, SLA is nozzle-free, setting it apart from other 3D printing methods. This feature eliminates the risk of nozzle clogs or filament feed issues which makes the printing process more reliable and uninterrupted [27,69,166]. Furthermore, objects produced through SLA generally exhibit smooth and highly detailed surface finishes [68,167]. The technique also excels in layer bonding due to its chemical curing process, resulting in strong layer-to-layer adhesion. This attribute is responsible for the high mechanical strength, structural integrity, and durability of printed objects [168].

The preparation of printable resins containing the right blend of active materials, photoinitiators, and monomers can be a complex process [27]. The flowability of the resin is another crucial consideration. If the flowability is not properly balanced, it can hinder the printing process and result in suboptimal print quality [27]. Additionally, the refractive index of the resin is of great importance. An unsuitable refractive index can cause UV light to scatter within the resin, which can result in defects, incomplete curing, compromised mechanical properties, and a lack of printing accuracy [27,162,169]. An unsuitable refractive index can cause UV light to scatter within the resin, which can result in defects, incomplete curing, compromised mechanical properties, and a lack of printing accuracy [27,162,169]. The SLA 3D printing system tends to be relatively expensive for industrial applications too [69]. The price per printed object, especially for simpler designs or smaller projects, might be comparable to those from other 3D printing methods. The overall affordability of SLA technology may vary depending on factors such as the complexity of the printed objects and the specific requirements of the application. Furthermore, post-processing requirements are often necessary for SLA prints. These post-processing steps, such as excess resin cleaning, can be time-consuming and may influence the final accuracy and surface finish of printed objects [28].

Some examples of SLA of batteries include:

He et al. developed a solid polymer electrolyte (SPE) containing lithium bis(trifluoromethanesulfonyl)imide (LiTFSI) for all-solid-state lithium metal batteries using SLA. The printed structure exhibited high ionic conductivity of 3.7×10^{-4} S cm^{-1}. At various charge rates, the discharge capacity decreased due to polarization; however, the 3D structure consistently outperformed other structures. Notably, the 3D structure exhibited an initial specific capacity of 166 mAh g^{-1} at 0.1 C, with higher capacity retention (78%) after

250 cycles compared to other structures (19%), and maintained a coulombic efficiency of approximately 100%. The obtained 3D-SPE replicate contained spiral walls with dimensions of 100 μm width, 150 μm height, and 200 μm spacing on a planar substrate of 100 μm thickness. This design ensured perfect adherence of the cathode to the electrolyte and enabled large-scale printing for practical applications. Further analysis revealed that the addition of succinonitrile (SCN) in the polymer resin weakened the mechanical strength of the electrolyte, resulting in decreased conductivity. The charge–discharge cycle demonstrated stability for at least 600 h without interruption. Moreover, the 3D structure exhibited lower impedance compared to other structures, which leads to improved cycling performance [87].

Chen et al. utilized SLA to fabricate a poly (ethylene glycol) (PEG)-base gel polymer electrolyte containing $LiClO_4$ salt. The cell was made using a 3D-printed solid electrolyte flown by LTO and LFP as electrodes. It was shown that the incorporation of solvated lithium salt into the polymer matrix facilitates lithium-ion transportation, particularly within the amorphous regions that led to improved mobility of polymer chains and higher ionic conductivity. The results indicated that the electrolyte can deliver high ionic conductivity of 4.8×10^{-3} S cm^{-1} with a discharge capacity of 1.4 μAh cm^{-2} over 2 cycles at 5 μA current, showing favorable interaction between the active material and the gel polymer electrolyte. It should be considered that cycling with a higher current (C/5) showed a gradual capacity decline over cycles, which led to failure by the 10th. It is likely due to lithium dendrite growth that causes short circuits. Some optimizations include adding SiO_2 to the electrolyte to suppress dendrites or applying PEG-based materials to the separator to enhance mechanical strength, improving cycling performance [170].

Norjely et al. employed SLA to fabricate a polyurethane acrylate (PUA)-based gel polymer electrolyte containing lithium perchlorate ($LiClO_4$) for solid-state lithium-ion batteries. The results showed the amorphous phase of the printed parts, which enhanced ionic conductivity by facilitating quicker segmental motion and bond rotations. Additionally, the higher concentration of $LiClO_4$ can alter the surface morphology from smooth to textured, resulting in enhanced Li^+ transportation and higher ionic conductivity. The ionic conductivity of the printed solid electrolyte with a 10 wt% $LiClO_4$ was equal to 1.24×10^{-3} S cm^{-1}, showing the method is promising for the fabrication of solid-state lithium-ion batteries. It should be considered that beyond 10 wt%, $LiClO_4$ recrystallization or agglomeration occurs, reducing free ions and diminishing ionic conductivity due to possible ion pair formation and Coulomb attraction-induced neutralization [171].

Zekoll et al. used SLA to create 3D templates from structured ceramic-polymer solid electrolytes made from $Li_{1.4}Al_{0.4}Ge_{1.6}$ $(PO_4)_3$ (LAGP). These electrolytes were composed of a 3D ceramic scaffold with channels filled with non-conducting polymers, including polypropylene or epoxy polymer followed by polymerization, which resulted in polymer-filled channels within the ceramic scaffold. High ionic conductivity of 1.6×10^{-4} S cm^{-1} along with high mechanical stability were achieved. The consistent density throughout the structure, which is achievable with designs such as the cube and diamond, is crucial for maintaining conductivity while minimizing the impact of non-conductive materials. These designs exhibited preferential fracture paths, which are beneficial for mechanical integrity [88].

Lee et al. employed DLP printing for making high-conductivity poly(ethylene oxide) (PEO) SPE. The structure was composed of a crosslinked polymer matrix that contained nanochannels filled with ionic liquid that exhibited high mechanical strength and an ionic conductivity of 3×10^{-4} S cm^{-1}. The results showed that increasing the volume fracture of the conductive component improves the ionic conductivity without sacrificing the mechanical strength. These structures are beneficial for use in customized applications of complex shapes [172].

Katsuyama et al. utilized SLA 3D printing and pyrolysis to fabricate hard carbon micro lattices with three different unit cell lengths (x) and beam widths (y) as a free-standing anode for sodium-ion batteries. The amount of shrinkage was about 70% in x and 75% in y

(Figure 5a). Charge–discharge profiles of samples with different sizes related to the beam width, where smaller samples corresponded to finer beams, revealed that finer structures exhibited higher capacity, reduced overpotential, and improved rate performance. Notably, the smallest sample exhibited the best behavior. Furthermore, areal capacity decreased with increasing charging rate, with degradation proportional to feature size. The galvanostatic intermittent titration technique (GITT) demonstrated that smaller beam widths led to decreased overpotential and variation in voltage. Additionally, XRD results of the samples after pyrolysis indicated low crystallinity due to the formation of hard carbon. Moreover, an interlayer distance of 3.79 Å was observed; this was larger than that of perfect graphite (3.35 Å) and resulted in increased ion storage capacity. As the results show, the highest specific capacity, which was related to the sample with the finer beam, was 225 mAh g^{-1} at 5 mA g^{-1}, with a coulombic efficiency of 80% in the initial cycle to 99.4% over the 2nd cycle. The capacity retention was about 80% over 100 cycles [173].

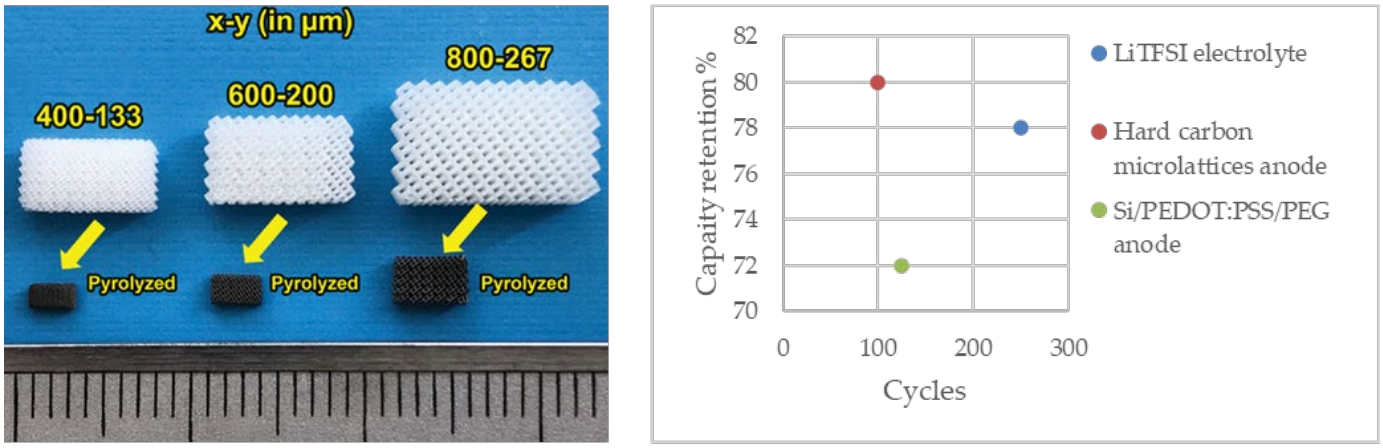

(a) (b)

Figure 5. (**a**) SLA-printed electrodes before and after pyrolysis. Reprinted/adapted with permission from Ref. [173]; published by Wiley, 2022 (**b**) capacity retention of the cells fabricated using SLA.

Ye et al. employed a DLP printer to fabricate a Si/PEDOT:PSS/PEG electrode with a Si content of 31.7 wt% for lithium-ion batteries to maximize energy storage while minimizing battery weight. PEDOT:PSS served as the conductive component, ensuring structural integrity and flexibility of the printed part. Battery performance demonstrated promise for silicon-based anodes, with an improved coulombic efficiency of up to 86.3% after 125 cycles and an initial discharge capacity of 1539 mAh g^{-1}. The reversible capacity reached 1105 mAh g^{-1} with 72% retention at 800 mA g^{-1} current density attributed to tolerance to mechanical stress. Despite conventional Si exhibiting high initial charge–discharge capacity (2560 mAh g^{-1} with 81.3% coulombic efficiency), 3D printed samples showed enhanced charge–discharge behavior compared to conventional Si electrodes. It is worth noting that the photograph from the printed parts illustrated the decreased transparency of the PEDOT:PSS/PEG by adding silicon, which impacts printability with high silicon load. Furthermore, viscosity analysis revealed increased viscosity with Si addition, limiting the amount of loaded silicon. SEM images depicted embedded and encapsulated Si primarily on the surface within a honeycomb design that provides more micropores and channel structures for Li ion diffusion. EIS analysis indicated lower charge transfer resistance for Si/PEDOT:PSS/PEG electrodes compared to the conventional Si electrodes, which suggests improved electrochemical performance [174].

Table 7 shows that until now, much of the research conducted on SLA printing of batteries focused on gel-based/solid electrolytes.

Table 7. Summary and comparison of electrochemical performance of SLA of batteries.

Printed Component	Electrochemical System	Discharge Capacity	Coulombic Efficiency	Cycle Numbers	Other Properties	Application	Reference
Electrolyte: LiTFSI	Anode: Li metal foil Cathode: LFP	166 mAh g^{-1} at 0.1 C	100%	250	Ionic conductivity: 3.7×10^{-4} S cm^{-1}	Lithium-ion battery	[87]
Electrolyte: PEG-base gel polymer	Anode: LTO Cathode: LFP	1.4 µAh cm^{-2} at 5 µA	N/A	2	Ionic conductivity: 4.8×10^{-3} S cm^{-1}	Lithium-ion battery	[170]
Electrolyte: PUA-base gel polymer	Stainless steel electrodes	N/A	N/A	N/A	Ionic conductivity: 1.24×10^{-3} S cm^{-1}	Lithium-ion battery	[171]
Electrolyte: LAGP solid electrolyte	Lithium electrodes	N/A	N/A	N/A	Ionic conductivity: 1.6×10^{-4} S cm^{-1}	Lithium-ion battery	[88]
Electrolyte: PEO solid electrolyte	Activated carbon-based electrodes coated on stainless steel	N/A	N/A	N/A	Ionic conductivity: 3×10^{-4} S cm^{-1}	Lithium battery systems, photovoltaic cells, supercapacitors, fuel cells	[172]
Anode: hard carbon micro lattices	Counter electrode: sodium metal foil Electrolyte: 1.0 m $NaPF_6$ in PC Separator: glass fiber filter	225 mAh g^{-1} at 5 mA g^{-1}	99.4%	2	N/A	Sodium-ion batteries	[173]
Anode: Si/PEDOT:PSS/PEG	Counter electrode: Li metal foil Electrolyte: LPF EC/DEC (v/v = 1/1) with 5% FEC Separator: Celgard 2400	1105 mAh g^{-1} at 800 mA g^{-1}	86.3%	125	N/A	Lithium-ion battery	[174]

Table 8 presents the parameters and processes associated with SLA printing. In this method, the presence of the active material and photoinitiator is important for printing battery components when the goal is to directly fabricate them through 3D printing.

Table 8. Key Parameters for the SLA process.

Resin Formulation	Printer Parameters	Fabrication Steps	Design	Reference
Active component: Lithium bis(trifluoromethanesulfonyl)imide (LiTFSI) Polymer resin: Poly(ethyleneglycol) diacrylate(PEGDA), SCN Photoinitiator: Phenylbis(2,4,6-trimethylbenzoyl)phosphine oxide	Light wavelength: 355 nm Power density: 10 W cm^{-2}	Resin preparation, 3D printing, drying in a vacuum oven at 25 °C for 2 h, further drying under Ar gas for 48 h	3D-Archimedean spiral structured	[87]
Active material: 1 M $LiClO_4$ Polymer resin: PEGDA Photoinitiator: Phenylbis(2,4,6-trimethylbenzoyl)phosphine oxide Photoabsorber: Sudan I	Printer resolution: 10 µm Layer thickness: 30 µm Exposure time: 13 s	Resin preparation, 3D printing	Zigzag shape	[170]
Active material: 1 M $LiClO_4$ Polymer resin: PUA	Light wavelength: 405 nm	Resin preparation, 3D printing	Circular disk	[171]
Polymer resin: photoresist IP-S	Light wavelength: 780 nm	3D printing of the template, LAGP synthesis, template immersion into LAGP, heat treatment to 900 °C for 5 h, impregnation of LAGP with polypropylene/Epoxy polymer	3D cubic bicontinuous microarchitectures	[88]
Polymer resin: photopolymer translucent Resin	Printer resolution: 50 µm First layer exposure time: 35 s Other layers exposure time: 2 s Light wavelength: 514 nm	3D printing, pyrolysis at 400 °C for 4 h and 1000 °C for 4 h	Lattice structure	[173]
Active material: silicon powder (30 wt%), PEDOT:PSS Polymer resin: PEG hydrogel Solvent: distilled water (DW) Photoinitiator: Bis(2,4,6-trimethylbenzoyl) phenylphosphineoxide (BAPO)	Printer resolution: 75 µm Laser spot diameter: 200 µm Light wavelength: 375 nm	Resin preparation, 3D printing, drying in a vacuum oven at 80 °C for 8 h	Honeycomb micropatterned	[174]

Figure 5b illustrates the capacity retention of the cells assembled using the SLA-printed battery component.

Furthermore, Table 9 summarizes the advantages and disadvantages of the abovementioned methods.

It is clear from this review of experimental results that closely align with theoretical electrochemical performance that 3D printing methods for battery fabrication are promising. There is potential for 3D printing to be incorporated into manufacturing high-performance batteries, primarily due to its inherent design freedom. One of the other interesting aspects of 3D printing batteries is the capability to fabricate solid-state electrolytes, which opens the path to developing all-solid-state batteries. This innovation could not only enhance battery performance but also enable the creation of fully 3D-printed batteries. Compared to batteries with liquid electrolytes, solid-state batteries often exhibit superior performance, particularly in the areas of safety.

Table 9. Advantages and disadvantages of DIW, FFF, IJP, and SLA.

Method	Advantages	Disadvantages
Direct Ink Writing	- High resolution - Affordable - Ease of use - Minimal post-production treatment - Flexibility in material selection - Multi-material printing	- Ink formulation - Material rheological properties optimization - Poor mechanical properties
Fused Filament Fabrication	- No need for ink preparation - Minimal waste - Economical - High production rates - Multi-material printing	- Filament formulation - Risk of nozzle clogging - Poor mechanical properties in z-direction - Low surface quality
InkJet Printing	- Affordable - Ease of use - Lower viscosity requirement - Flexibility in material selection - Multi-material printing	- Nonuniform printed structure - Ink formulation
Stereolithography	- High resolution - Nozzle-free printing process - Smooth and highly detailed surface finishes - Strong layer-to-layer adhesion - High mechanical strength - Structural integrity - Durability	- Resin formulation - Resin flowability - Resin refractive index for resin - Relatively high cost for industrial applications - Post-processing requirements

It is also clear from this review that a range of 3D printing methods can be used for various battery components. In this regard, DIW and IJP enable the loading of active and conductive materials into printable ink to facilitate the production of desired components. On the other hand, FFF offers a customizable approach by loading these materials into filaments. Additionally, compared to the other methods, it can be seen that for SLA, substantial research has been focused primarily on the fabrication of solid electrolytes. Nevertheless, the successful fabrication of other battery components, including free-standing anodes [173], demonstrates SLA's potential in broadening battery component fabrication.

3D printing has proven its ability to fabricate battery components using high-performance materials. Silicon, for example, as a major byproduct of the solar photovoltaic (PV) industry [175], stands out as a promising anode material due to its high theoretical capacity (around 3579 mAh g^{-1}) [176]. The primary challenge associated with utilizing silicon as an anode is the substantial volume change experienced by the material during battery cycling, thereby constraining its application. Various 3D printing methods, including DIW [120], FFF [144], IJP [156], and SLA [174], have successfully produced silicon anodes with high electrochemical performance by addressing the volume change issue through special structures achievable via 3D printing, as well as by adding carbon additives that can accommodate the volume change in silicon by covering it. Finally, the high resolution and high fabrication rate of SLA as well as the capability to fabricate solid electrolytes and silicon anodes makes it an exceptionally promising candidate for the production of all-solid-state batteries with superior electrochemical performance, as well as high safety, efficiency, and sustainability. Therefore, among various 3D printing methods, the SLA method is particularly promising for battery fabrication. Challenges, however, remain related to the non-conductive and non-active polymer resin and cost considerations. In this regard, the adoption of the free and open-source hardware (FOSH) development of

scientific tools approach is promising as it has been shown to decrease capital costs by about 90% on average [177]. Specific technologies for battery research can be extremely cost-effective. For example, a USD 20,000 potentiostat and galvanostat used for characterizing thin-film batteries can be replaced with a USD 100 open-source tool [178]. In addition, open battery management is also available [179], including for in situ monitoring of Li-ion cells [180]. There has also been more application-specific FOSH such as a maintenance tool for light-EV batteries [181]. Finally, there has been work to make completely all-iron batteries FOSH [182,183], which provides a model for the FOSH 3D printable batteries discussed here. Integrating an open-source toolchain, spanning from material preparation to battery packaging, emerges as a promising approach to reduce fabrication costs and enhance accessibility to 3D printing technologies for battery research and production.

4. Conclusions

The advent of 3D printing marks a potential transformative shift in the fabrication of energy storage devices as it introduces new potential for rapid innovation and customization of batteries for specific applications. In contrast to traditional manufacturing, the precision of 3D printing coupled with geometrical freedom can be used to improve battery performance and offer more efficient energy storage solutions. Notably, as shown in this review, 3D printing of batteries offers a path to higher energy density, capacity, and overall performance compared to conventional manufacturing techniques. Overall, the evidence presented through numerous case studies from labs making substantial progress all over the world shows the potential of 3D printing as a promising solution to enhance energy storage capabilities. Furthermore, the design freedom of 3D printing makes the fabrication of complex geometries and structures possible and emerges as another key aspect to improve energy storage capacities and applications in the future. In addition, 3D printing is a promising method for enabling the use of new materials for battery fabrication to improve battery performance. From an environmental protection viewpoint, the waste reduction associated with the 3D printing of batteries is a way toward a more environmentally friendly future. Indirectly, the improved performance and flexibility in applications as well as the potential to reduce energy storage costs could have a substantial positive impact in enabling intermittent renewable energy sources to displace fossil fuels. As 3D printing technologies become more accessible, the prospect of cost-effective production for customized batteries is extremely promising.

Author Contributions: Conceptualization, M.M. and J.M.P.; methodology, M.M. and J.M.P.; formal analysis, M.M. and J.M.P.; investigation, M.M. and J.M.P.; resources, M.M. and J.M.P.; data curation, M.M. and J.M.P.; writing—original draft preparation, M.M. and J.M.P.; writing—review and editing, M.M. and J.M.P.; visualization, M.M.; supervision, J.M.P.; project administration, J.M.P.; funding acquisition, J.M.P. All authors have read and agreed to the published version of the manuscript.

Funding: This study was supported by the Thompson Endowments and the Natural Sciences and Engineering Research Council of Canada.

Conflicts of Interest: The authors declare no conflicts of interest.

Appendix A

Appendix A.1. Battery Basics

The following basic definitions of battery terms are provided from established references in the field [184–186].

Appendix A.1.1. Energy

Energy density is the amount of energy stored in a given volume or mass that defines the battery capacity. The specific energy density or the gravimetric energy density is the energy of a specific weight measured in Wh/kg and the volumetric energy density is the energy stored in a specific volume measured in Wh/m^3.

Appendix A.1.2. Power

Power density is the rate at which energy is transferred within the battery structure and is particularly crucial in applications such as electric vehicles where rapid energy delivery is required. Specific power density refers to the rate at which a battery can deliver electrical power relative to its weight and quantifies how quickly a battery can discharge its stored energy, typically measured in watts per unit of weight (W/kg). Volumetric power density signifies the rate at which a battery can deliver electrical power relative to its volume and is measured in watts per unit of volume (W/m^3).

Appendix A.1.3. Voltage

Nominal voltage indicates the average voltage value assigned to a particular type or model of battery for design and specification purposes. It is often used as a reference point and does not reflect the actual voltage of the battery at any specific moment during its operation. Open circuit voltage (OCV or V_{OC}) is the voltage across the battery terminals when no current is flowing. It represents the potential difference between the positive and negative terminals in the absence of a load and is an indicator of the SOC.

Appendix A.1.4. State of the Charge (SOC)

SOC is the amount of energy stored in a battery at a given moment and is expressed as a percentage (%) of the total capacity. It indicates how much charge is available for use.

Appendix A.1.5. Capacity

Total capacity represents the maximum number of ampere-hours that can be extracted from a fully charged battery cell before it is fully discharged. This limit is determined by the SOC and involves discharging from 100% to 0%. Discharge capacity is the number of ampere-hours that can be drawn from a fully charged cell at a constant current rate, stopping before encountering a minimum voltage limit. Unlike total capacity, it does not indicate the complete charge a cell can hold, as it discharges from 100% to a minimum voltage. Reversible charge capacity refers to the amount of charge that can be cyclically stored and released in a reversible electrochemical reaction and indicates the stability of the electrochemical process.

Appendix A.1.6. Voltage Drops

- There are several potential mechanisms that result in voltage drops. First, activation loss happens due to the slow nature of the reactions that occur on the electrode surface. Fuel crossover and internal currents result from electrons passing through the electrolyte, which leads to charge loss in this way. Ohmic loss, or internal resistance, is the energy loss resulting from resistance to the flow of electrons through electrode materials and interconnections, as well as resistance to the flow of ions through the electrolyte. Mass transport (concentration) loss occurs when the electrode surface is depleted from charges over time, and reactants require time to diffuse from the inner bulk to the surface for the reaction to keep on.

Appendix A.1.7. Self-Discharge

Self-discharge is the result of unwanted chemical reactions that occur internally, leading to various issues such as current leakage, dendrite formation, electrolyte decomposition, and electrode decomposition. These processes contribute to the gradual discharge of a battery even when it is not in use.

Appendix A.1.8. Electrical Double Layer

During battery operation, the charged electrodes interface with the electrolyte resulting in the formation of a layer of charges. This occurs due to the attractive forces between the

charged electrode surface and the ions present in the electrolyte, and it is referred to as the electrical double layer.

Appendix A.1.9. Lithiation/De-lithiation

Lithiation describes the insertion of lithium ions into the anode and de-lithiation refers to the removal from the anode during the charging and discharging of a lithium-ion battery, respectively.

Appendix A.1.10. Particle Pulverization

Particle pulverization in lithium-ion batteries refers to the mechanical fragmentation or disintegration of electrode materials, especially in the anode, as a result of repeated cycles of lithium-ion intercalation and deintercalation during charging and discharging.

Appendix A.1.11. Lithium Plating

When the battery voltage exceeds a certain threshold during charging, the excess voltage drives the reduction of lithium ions at the anode surface, leading to the deposition of metallic lithium, which is more likely to occur at low temperatures; lower temperatures reduce lithium-ion mobility and make it easier for lithium ions to deposit as solid lithium on the anode surface, which is called lithium plating.

Appendix A.1.12. Solid Electrolyte Interface (SEI)

During the initial cycle, the electrolyte containing lithium salt decomposes to create reactive species. These reactive species, along with the lithium ions, precipitate on the anode surface. This ongoing process results in the formation of multiple layers with different chemical compositions and properties. Maintaining an optimum thickness in this layer is crucial as it can provide mechanical stability and prevent further decomposition. It is essential, however, for this layer to be thin enough not to reduce ionic conductivity.

Appendix A.1.13. Charge–Discharge Test

The charge–discharge test involves applying a constant current while considering the cut-off voltage and scan rate. During charging, the constant current leads to an increase in potential until the cut-off voltage is reached. Then, the current is reversed and the potential starts to decrease to the minimum cut-off voltage. This test is a fundamental method for evaluating the capacity, reversibility, stability, and rate capability of the battery.

Appendix A.1.14. Cyclic Voltammetry Test

This test involves tracking the current by linearly sweeping the voltage over time at a specified scan rate, which is higher than that used in charge–discharge cycles. The reason for this is that the test is employed to study the redox reactions, reaction kinetics, and electrochemical behavior of the materials within the battery.

Appendix A.1.15. Electrochemical Impedance Spectroscopy (EIS)

EIS is a test that measures various impedance elements in a battery system by applying a small alternating current across a wide range of frequencies and measuring the corresponding response. The output of the test is a plot called the Nyquist plot, which is made of the real part of the impedance on the x-axis and the imaginary part of the impedance on the y-axis. An equivalent circuit is constructed from a Nyquist plot in order to model and analyze the electrochemical behavior of a system. Different parts of the curve can be explained as follows:

- Ohmic resistance (Rs) is related to the ionic and electronic conductivity of various components in the battery, including the electrolyte, electrodes, and current collector. This is measured at low frequencies, and on the Nyquist plot, it is represented by the real part of the impedance (Figure A1a).

- Charge transfer resistance (Rct) is the resistance related to the electrochemical reactions occurring at the interface layer of the electrode–electrolyte. Information about the kinetics of the charge transfer process, such as lithium intercalation at the electrode surface, is provided by this resistance. On the Nyquist plot, this resistance is observed as a semicircle, with the radius of the semicircle representing the charge transfer resistance. This region corresponds to the high-frequency range. An improvement in battery performance is indicated by a reduction in the radius/diameter of this semicircle, suggesting that the charge transfer processes at the electrode–electrolyte interface are more efficient and faster. This layer also serves as a capacitance that stores charges transferring slowly to the electrode. In the equivalent circuit, it is represented as a capacitance in parallel to the charge transfer resistance (Figure A1b).
- Warburg impedance (W) is related to the diffusion (mass transport) of lithium ions into the solid electrode and electrolyte. On the Nyquist plot, it is represented by a sloped line. This region corresponds to the medium frequency range on the plot. The slope of the line reflects the diffusion coefficient of the species. A steeper slope indicates more difficult ion diffusion, while a shallower slope suggests easier mass transport and diffusion. The tail of this impedance is also significant. Tail extensions or deviations from the line indicate additional electrochemical processes occurring in the battery (Figure A1c).

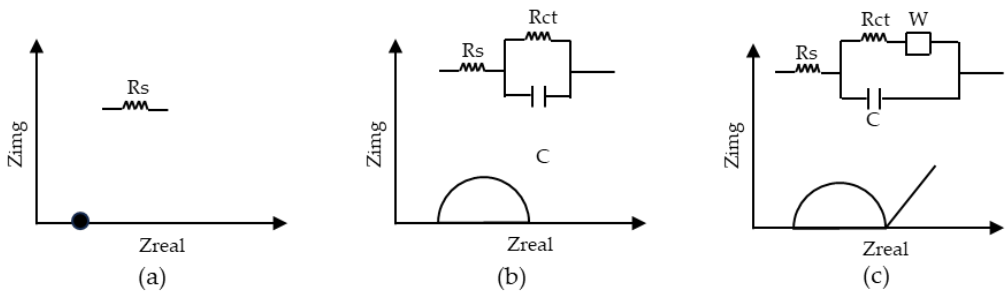

Figure A1. Nyquist plot, (**a**) Ohmic resistance, (**b**) Charge transfer resistance, and (**c**) Warburg resistance.

Appendix A.2. Basic Types of Batteries

In general, batteries are divided into two categories: primary and secondary batteries. Primary batteries, also known as disposable or non-rechargeable batteries, are designed for single-use applications. They provide a reliable source of power by converting chemical energy into electrical energy. Common examples include zinc–carbon, alkaline zinc–manganese dioxide, and metal–air batteries [187]. Primary batteries are used for low and intermittent power needs, such as remote controls and smoke detectors [188]. They are however, one of the most expensive sources of electric energy and in general should be replaced by secondary batteries [189]. Secondary batteries are rechargeable batteries that can be reused multiple times by reversing the chemical reactions through an external power source, like a charger. Popular secondary battery types include lead acid, nickel–cadmium (NiCd), nickel–metal hydride (Ni–MH), and lithium-ion (Li-ion) batteries [190,191]. They are widely used in portable electronics like smartphones, laptops, and electric vehicles, offering cost-effective and eco-friendly alternatives to disposable batteries while reducing long-term waste [192,193].

Appendix A.2.1. Lead–Acid

A lead–acid battery consists of a lead dioxide (PbO_2) anode and a cathode composed of sponge-like lead (Pb), while its electrolyte is made of cost-effective, non-flammable sulfuric acid [190]. During the discharge of lead acid batteries, the lead ions (Pb^{2+}) within the battery engage in a chemical reaction with the electrolyte, leading to the formation

of lead sulfate ($PbSO_4$) crystals. During the charging process, these crystals undergo a transformation, reverting to their elemental states as Pb and PbO_2 [190].

The lead–acid battery has benefits, including a long cycle life of up to 1500–5000 cycles [32]. These batteries are also known for their recyclability and cost-effectiveness, which holds the largest market share among rechargeable batteries in the automotive industry, primarily due to the abundance of raw materials [190,194,195]. Nevertheless, one of the major concerns about these batteries is toxicity [196]. Moreover, these batteries tend to be relatively heavy and have an energy density within the range of 30–50 Wh/kg, which is not high compared to the other rechargeable batteries [197]. The open circuit voltage of lead–acid batteries remains stable at 2.1 volts [190]. It is also worth mentioning that they lack fast-charging capabilities and do not offer a high depth of discharge [190]. Additionally, the coulombic efficiencies of these batteries are 90–95% [198].

Appendix A.2.2. NiCd

NiCd batteries consist of a metallic Cd anode, a nickel hydroxide ($Ni(OH)_2$) cathode, and an aqueous potassium hydroxide (KOH) electrolyte [199,200]. During the discharge, OH^- and $Ni(OH)_2$ on the cathode side and $Cd(OH)_2$ on the anode side are produced. This reaction reverses during the charging process [201].

NiCd batteries have several advantages. Notably, the NiCd battery offers an energy density ranging from 50 to 75 Wh/kg [194], and a long cycle life that spans from 3500 to 50,000 cycles [202], with a coulombic efficiency of 70–80% [198]. It has resilience under mechanical and electrical stress [194], does not release gas [200], has a high depth of discharge, and is suitable for a wide range of industrial applications, including remote controls, aircraft, and diesel engine starters [203]. The main drawbacks of these batteries are the cost [194], and the toxic and heavy materials [204]. Additionally, NiCd batteries suffer from a relatively high self-discharge rate. The open circuit voltage of the nickel–cadmium battery is 1.2 Volts [205].

Appendix A.2.3. Ni–MH

Ni–MH batteries are made of a nickel hydroxide anode, a metal hydride cathode, and an electrolyte based on aqueous potassium hydroxide [206]. Hydroxide ions are generated at the negative electrode through the decomposition of water within the electrolyte, while the positive electrode experiences oxidation of the nickel hydroxide [207].

The Ni–MH battery has a high energy density of more than 70 Wh/kg, a power density of more than 200 W/kg, and a broad operational temperature range [208]. It is often considered a safe and environmentally friendly option [209]. Furthermore, its lifespan is high, typically reaching up to 3000 cycles [210], and the coulombic efficiency is 70–80% [198]. The Ni–MH battery has a notable self-discharge rate and a limited DOD [211,212]. The open circuit voltage of the Ni–MH battery is between 1.25 and 1.35 V [213].

Appendix A.2.4. Li-Ion

Lithium-ion batteries typically consist of a graphitic carbon anode with a layer structure. The cathode in these batteries is made of lithiated metal oxide compounds, including lithium cobaltite (LCO), mixed oxides of nickel, cobalt, and aluminum (NCA), nickel, cobalt, and manganese (NCM), lithium manganese dioxide spinel (LMO), and lithium iron phosphate (LFP) [214]. The electrolyte is also a solution of lithium salts dissolved in organic carbonates [214]. During the charging process, lithium atoms within the cathode transform into lithium ions and migrate towards the carbon-based anode, depositing on the anode surface as lithium atoms [204]. Additionally, these batteries perform with a high coulombic efficiency of more than 95% [198].

Lithium-ion batteries have benefits, including a long cycle life of up to 3000 cycles, high energy density ranging from 75 to 125 Wh/kg [215], and minimal self-discharge [216]. Lithium-ion batteries are, however, sensitive to overvoltage [199]. Their open circuit voltage typically falls within the range of 3 to 4.2 volts [217].

References

1. Electricity in the U.S.—U.S. Energy Information Administration (EIA). Available online: https://www.eia.gov/energyexplained/electricity/electricity-in-the-us.php (accessed on 19 January 2024).
2. Pearce, J.M.; Parncutt, R. Quantifying Global Greenhouse Gas Emissions in Human Deaths to Guide Energy Policy. *Energies* **2023**, *16*, 6074. [CrossRef]
3. D'Amato, G.; Cecchi, L. Effects of Climate Change on Environmental Factors in Respiratory Allergic Diseases. *Clin. Exp. Allergy* **2008**, *38*, 1264–1274. [CrossRef] [PubMed]
4. Haines, A.; Kovats, R.; Campbell-Lendrum, D.; Corvalan, C. Climate Change and Human Health: Impacts, Vulnerability, and Mitigation. *Lancet* **2006**, *367*, 2101–2109. [CrossRef] [PubMed]
5. Denkenberger, D.C.; Pearce, J.M. Feeding Everyone: Solving the Food Crisis in Event of Global Catastrophes That Kill Crops or Obscure the Sun. *Futures* **2015**, *72*, 57–68. [CrossRef]
6. Barnes, D.F.; Floor, W.M. Rural Energy in Developing Countries: A Challenge for Economic Development. *Annu. Rev. Energy Environ.* **1996**, *21*, 497–530. [CrossRef]
7. Stern, N.H.; Treasury, G.B. *The Economics of Climate Change: The Stern Review*; Cambridge University Press: Cambridge, UK, 2007; ISBN 978-0-521-70080-1.
8. Peters, G.P.; Hertwich, E.G. CO_2 Embodied in International Trade with Implications for Global Climate Policy. *Environ. Sci. Technol.* **2008**, *42*, 1401–1407. [CrossRef] [PubMed]
9. Heidari, N.; Pearce, J.M. A Review of Greenhouse Gas Emission Liabilities as the Value of Renewable Energy for Mitigating Lawsuits for Climate Change Related Damages. *Renew. Sustain. Energy Rev.* **2016**, *55*, 899–908. [CrossRef]
10. Pryor, S.C.; Barthelmie, R.J. Climate Change Impacts on Wind Energy: A Review. *Renew. Sustain. Energy Rev.* **2010**, *14*, 430–437. [CrossRef]
11. Global Wind and Solar Energy Share in Electricity Mix 2022. Available online: https://www.statista.com/statistics/1302047/global-wind-and-solar-energy-share-electricity-mix/ (accessed on 26 September 2023).
12. SDG Knowledge Hub. Wind and Solar Will Provide 50% of Electricity in 2050, BNEF Report Finds. Available online: https://sdg.iisd.org/news/wind-and-solar-will-provide-50-of-electricity-in-2050-bnef-report-finds/ (accessed on 19 January 2024).
13. Yu, H.; Helland, H.; Yu, X.; Gundersen, T.; Sin, G. Optimal Design and Operation of an Organic Rankine Cycle (ORC) System Driven by Solar Energy with Sensible Thermal Energy Storage. *Energy Convers. Manag.* **2021**, *244*, 114494. [CrossRef]
14. Ali, U. Bloomberg New Energy Outlook 2019: The Future of the Energy Sector. Available online: https://www.power-technology.com/news/bloomberg-new-energy-outlook-2019-2/ (accessed on 26 September 2023).
15. Adeh, E.H.; Good, S.P.; Calaf, M.; Higgins, C.W. Solar PV Power Potential Is Greatest Over Croplands. *Sci. Rep.* **2019**, *9*, 11442. [CrossRef]
16. Garg, P.; Orosz, M.S.; Kumar, P. Thermo-Economic Evaluation of ORCs for Various Working Fluids. *Appl. Therm. Eng.* **2016**, *109*, 841–853. [CrossRef]
17. Zhu, Z.; Jiang, T.; Ali, M.; Meng, Y.; Jin, Y.; Cui, Y.; Chen, W. Rechargeable Batteries for Grid Scale Energy Storage. *Chem. Rev.* **2022**, *122*, 16610–16751. [CrossRef]
18. Kebede, A.A.; Kalogiannis, T.; Van Mierlo, J.; Berecibar, M. A Comprehensive Review of Stationary Energy Storage Devices for Large Scale Renewable Energy Sources Grid Integration. *Renew. Sustain. Energy Rev.* **2022**, *159*, 112213. [CrossRef]
19. Harper, G.; Sommerville, R.; Kendrick, E.; Driscoll, L.; Slater, P.; Stolkin, R.; Walton, A.; Christensen, P.; Heidrich, O.; Lambert, S.; et al. Recycling Lithium-Ion Batteries from Electric Vehicles. *Nature* **2019**, *575*, 75–86. [CrossRef] [PubMed]
20. Nair, N.-K.C.; Garimella, N. Battery Energy Storage Systems: Assessment for Small-Scale Renewable Energy Integration. *Energy Build.* **2010**, *42*, 2124–2130. [CrossRef]
21. Joseph, P.K.; Devaraj, E. Design of Hybrid Forward Boost Converter for Renewable Energy Powered Electric Vehicle Charging Applications. *IET Power Electron.* **2019**, *12*, 2015–2021. [CrossRef]
22. Ransome, T. Lithium Ion Battery. Available online: https://www.renewables4u.com.au/lithium-ion-battery/ (accessed on 19 January 2024).
23. Mottaghi, M.; Rahman, M.; Kulkarni, A.; Pearce, J.M. AC/off-Grid Photovoltaic Powered Open-Source Ball Mill. *HardwareX* **2023**, *14*, e00423. [CrossRef] [PubMed]
24. Mottaghi, M.; Bai, Y.; Kulkarni, A.; Pearce, J.M. Open Source Scientific Bottle Roller. *HardwareX* **2023**, *15*, e00445. [CrossRef]
25. Dhankani, K.C.; Pearce, J.M. Open Source Laboratory Sample Rotator Mixer and Shaker. *HardwareX* **2017**, *1*, 1–12. [CrossRef]
26. Vadivel, D.; Branciforti, D.S.; Kerroumi, O.; Dondi, M.; Dondi, D. Mostly 3D Printed Chemical Synthesis Robot. *HardwareX* **2022**, *11*, e00310. [CrossRef]
27. Wittbrodt, B.T.; Glover, A.G.; Laureto, J.; Anzalone, G.C.; Oppliger, D.; Irwin, J.L.; Pearce, J.M. Life-Cycle Economic Analysis of Distributed Manufacturing with Open-Source 3-D Printers. *Mechatronics* **2013**, *23*, 713–726. [CrossRef]
28. Pearce, J.M. *Open-Source Lab: How to Build Your Own Hardware and Reduce Research Costs*; Elsevier: Amsterdam, The Netherlands, 2013; ISBN 978-0-12-410486-0.
29. Laplume, A.O.; Petersen, B.; Pearce, J.M. Global Value Chains from a 3D Printing Perspective. *J. Int. Bus. Stud.* **2016**, *47*, 595–609. [CrossRef]
30. Lyu, Z.; Lim, G.J.H.; Koh, J.J.; Li, Y.; Ma, Y.; Ding, J.; Wang, J.; Hu, Z.; Wang, J.; Chen, W.; et al. Design and Manufacture of 3D-Printed Batteries. *Joule* **2021**, *5*, 89–114. [CrossRef]

31. Pang, Y.; Cao, Y.; Chu, Y.; Liu, M.; Snyder, K.; MacKenzie, D.; Cao, C. Additive Manufacturing of Batteries. *Adv. Funct. Mater.* **2020**, *30*, 1906244. [CrossRef]
32. Tagawa, K.; Brodd, R.J. Production Processes for Fabrication of Lithium-Ion Batteries. In *Lithium-Ion Batteries: Science and Technologies*; Yoshio, M., Brodd, R.J., Kozawa, A., Eds.; Springer: New York, NY, USA, 2009; pp. 181–194. ISBN 978-0-387-34445-4.
33. Bommineedi, L.K.; Upadhyay, N.; Minnes, R. Screen Printing: An Ease Thin Film Technique. In *Simple Chemical Methods for Thin Film Deposition: Synthesis and Applications*; Sankapal, B.R., Ennaoui, A., Gupta, R.B., Lokhande, C.D., Eds.; Springer Nature: Singapore, 2023; pp. 449–507. ISBN 978-981-9909-61-2.
34. Wei, T.-S.; Ahn, B.Y.; Grotto, J.; Lewis, J.A. 3D Printing of Customized Li-Ion Batteries with Thick Electrodes. *Adv. Mater.* **2018**, *30*, 1703027. [CrossRef] [PubMed]
35. Shi, H.; Cao, J.; Sun, Z.; Ghazi, Z.A.; Zhu, X.; Han, S.; Ren, D.; Lu, G.; Lan, H.; Li, F. 3D Printing Enables Customizable Batteries. *Batter. Supercaps* **2023**, *6*, e202300161. [CrossRef]
36. Idrees, M.; Batool, S.; Din, M.A.U.; Javed, M.S.; Ahmed, S.; Chen, Z. Material-Structure-Property Integrated Additive Manufacturing of Batteries. *Nano Energy* **2023**, *109*, 108247. [CrossRef]
37. Gonçalves, R.; Lanceros-Méndez, S.; Costa, C.M. Electrode Fabrication Process and Its Influence in Lithium-Ion Battery Performance: State of the Art and Future Trends. *Electrochem. Commun.* **2022**, *135*, 107210. [CrossRef]
38. Fonseca, N.; Thummalapalli, S.V.; Jambhulkar, S.; Ravichandran, D.; Zhu, Y.; Patil, D.; Thippanna, V.; Ramanathan, A.; Xu, W.; Guo, S.; et al. 3D Printing-Enabled Design and Manufacturing Strategies for Batteries: A Review. *Small* **2023**, *19*, 2302718. [CrossRef]
39. Ben-Barak, I.; Schneier, D.; Kamir, Y.; Goor, M.; Golodnitsky, D.; Peled, E. Drop-on-Demand 3D-Printed Silicon-Based Anodes for Lithium-Ion Batteries. *J. Solid State Electrochem.* **2022**, *26*, 183–193. [CrossRef]
40. Ben-Barak, I.; Kamir, Y.; Menkin, S.; Goor, M.; Shekhtman, I.; Ripenbein, T.; Galun, E.; Golodnitsky, D.; Peled, E. Drop-on-Demand 3D Printing of Lithium Iron Phosphate Cathodes. *J. Electrochem. Soc.* **2018**, *166*, A5059. [CrossRef]
41. Gao, X.; Liu, K.; Su, C.; Zhang, W.; Dai, Y.; Parkin, I.P.; Carmalt, C.J.; He, G. From Bibliometric Analysis: 3D Printing Design Strategies and Battery Applications with a Focus on Zinc-Ion Batteries. *SmartMat* **2024**, *5*, e1197. [CrossRef]
42. Torabi, F.; Ahmadi, P. Battery Technologies. In *Simulation of Battery Systems*; Elsevier: Amsterdam, The Netherlands, 2020; pp. 1–54. ISBN 978-0-12-816212-5.
43. Delannoy, P.-E.; Riou, B.; Brousse, T.; Le Bideau, J.; Guyomard, D.; Lestriez, B. Ink-Jet Printed Porous Composite $LiFePO_4$ Electrode from Aqueous Suspension for Microbatteries. *J. Power Sources* **2015**, *287*, 261–268. [CrossRef]
44. Zhou, L.; Ning, W.; Wu, C.; Zhang, D.; Wei, W.; Ma, J.; Li, C.; Chen, L. 3D-Printed Microelectrodes with a Developed Conductive Network and Hierarchical Pores toward High Areal Capacity for Microbatteries. *Adv. Mater. Technol.* **2019**, *4*, 1800402. [CrossRef]
45. Wang, Y.; Chen, C.; Xie, H.; Gao, T.; Yao, Y.; Pastel, G.; Han, X.; Li, Y.; Zhao, J.; Fu, K.; et al. 3D-Printed All-Fiber Li-Ion Battery toward Wearable Energy Storage. *Adv. Funct. Mater.* **2017**, *27*, 1703140. [CrossRef]
46. Huang, J.; Yang, J.; Li, W.; Cai, W.; Jiang, Z. Electrochemical Properties of $LiCoO_2$ Thin Film Electrode Prepared by Ink-Jet Printing Technique. *Thin Solid Films* **2008**, *516*, 3314–3319. [CrossRef]
47. Dudney, N.J.; Neudecker, B.J. Solid State Thin-Film Lithium Battery Systems. *Curr. Opin. Solid State Mater. Sci.* **1999**, *4*, 479–482. [CrossRef]
48. Schwenzel, J.; Thangadurai, V.; Weppner, W. Developments of High-Voltage All-Solid-State Thin-Film Lithium Ion Batteries. *J. Power Sources* **2006**, *154*, 232–238. [CrossRef]
49. Clement, B.; Lyu, M.; Sandeep Kulkarni, E.; Lin, T.; Hu, Y.; Lockett, V.; Greig, C.; Wang, L. Recent Advances in Printed Thin-Film Batteries. *Engineering* **2022**, *13*, 238–261. [CrossRef]
50. Ding, J.; Shen, K.; Du, Z.; Li, B.; Yang, S. 3D-Printed Hierarchical Porous Frameworks for Sodium Storage. *ACS Appl. Mater. Interfaces* **2017**, *9*, 41871–41877. [CrossRef]
51. Gupta, V.; Alam, F.; Verma, P.; Kannan, A.M.; Kumar, S. Additive Manufacturing Enabled, Microarchitected, Hierarchically Porous Polylactic-Acid/Lithium Iron Phosphate/Carbon Nanotube Nanocomposite Electrodes for High Performance Li-Ion Batteries. *J. Power Sources* **2021**, *494*, 229625. [CrossRef]
52. Saleh, M.S.; Li, J.; Park, J.; Panat, R. 3D Printed Hierarchically-Porous Microlattice Electrode Materials for Exceptionally High Specific Capacity and Areal Capacity Lithium Ion Batteries. *Addit. Manuf.* **2018**, *23*, 70–78. [CrossRef]
53. Liu, C.; Qiu, Y.; Liu, Y.; Xu, K.; Zhao, N.; Lao, C.; Shen, J.; Chen, Z. Novel 3D Grid Porous $Li_4Ti_5O_{12}$ Thick Electrodes Fabricated by 3D Printing for High Performance Lithium-Ion Batteries. *J. Adv. Ceram.* **2022**, *11*, 295–307. [CrossRef]
54. Liu, C.; Cheng, X.; Li, B.; Chen, Z.; Mi, S.; Lao, C. Fabrication and Characterization of 3D-Printed Highly-Porous 3D $LiFePO_4$ Electrodes by Low Temperature Direct Writing Process. *Materials* **2017**, *10*, 934. [CrossRef] [PubMed]
55. Martinez, A.C.; Maurel, A.; Aranzola, A.P.; Grugeon, S.; Panier, S.; Dupont, L.; Hernandez-Viezcas, J.A.; Mummareddy, B.; Armstrong, B.L.; Cortes, P.; et al. Additive Manufacturing of $LiNi_{1/3}Mn_{1/3}Co_{1/3}O_2$ Battery Electrode Material via Vat Photopolymerization Precursor Approach. *Sci. Rep.* **2022**, *12*, 19010. [CrossRef]
56. Yang, Q.; Liu, Q.; Ling, W.; Dai, H.; Chen, H.; Liu, J.; Qiu, Y.; Zhong, L. Porous Electrode Materials for Zn-Ion Batteries: From Fabrication and Electrochemical Application. *Batteries* **2022**, *8*, 223. [CrossRef]
57. Yang, Y.; Ai, L.; Yu, S.; He, J.; Xu, T.; Chen, D.; Shen, L. 3D-Printed Porous GO Framework Enabling Dendrite-Free Lithium-Metal Anodes. *ACS Appl. Energy Mater.* **2022**, *5*, 15666–15672. [CrossRef]

58. Chen, C.; Li, S.; Notten, P.H.L.; Zhang, Y.; Hao, Q.; Zhang, X.; Lei, W. 3D Printed Lithium-Metal Full Batteries Based on a High-Performance Three-Dimensional Anode Current Collector. *ACS Appl. Mater. Interfaces* **2021**, *13*, 24785–24794. [CrossRef]
59. Zhang, M.; Li, L.; Lin, Q.; Tang, M.; Wu, Y.; Ke, C. Hierarchical-Coassembly-Enabled 3D-Printing of Homogeneous and Heterogeneous Covalent Organic Frameworks. *J. Am. Chem. Soc.* **2019**, *141*, 5154–5158. [CrossRef]
60. Mu, Y.; Chu, Y.; Pan, L.; Wu, B.; Zou, L.; He, J.; Han, M.; Zhao, T.; Zeng, L. 3D Printing Critical Materials for Rechargeable Batteries: From Materials, Design and Optimization Strategies to Applications. *Int. J. Extrem. Manuf.* **2023**, *5*, 042008. [CrossRef]
61. Menon, A.; Khan, A.; Balakrishnan, N.T.M.; Raghavan, P.; Leon Y Leon, C.A.; Khan, H.A.; Fatima, M.J.J.; Owuor, P.S. Advances in 3D Printing for Electrochemical Energy Storage Systems. *J. Mater. Sci. Technol. Res.* **2021**, *8*, 50–69. [CrossRef]
62. Thakur, A.R.; Dong, X. Experimental and Numerical Studies of Slurry-Based Coextrusion Deposition of Continuous Carbon Fiber Micro-Batteries to Additively Manufacture 3D Structural Battery Composites. *Compos. Part B Eng.* **2023**, *255*, 110632. [CrossRef]
63. Cheng, M. Direct Ink Writing of Polymer Batteries. Ph.D. Thesis, University of Illinois at Chicago, Chicago, IL, USA, 2020.
64. Ragones, H.; Menkin, S.; Kamir, Y.; Gladkikh, A.; Mukra, T.; Kosa, G.; Golodnitsky, D. Towards Smart Free Form-Factor 3D Printable Batteries. *Sustain. Energy Fuels* **2018**, *2*, 1542–1549. [CrossRef]
65. Ponnada, S.; Babu Gorle, D.; Chandra Bose, R.S.; Sadat Kiai, M.; Devi, M.; Venkateswara Raju, C.; Baydogan, N.; Kar Nanda, K.; Marken, F.; Sharma, R.K. Current Insight into 3D Printing in Solid-State Lithium-Ion Batteries: A Perspective. *Batter. Supercaps* **2022**, *5*, e202200223. [CrossRef]
66. Nyika, J.; Mwema, F.M.; Mahamood, R.M.; Akinlabi, E.T.; Jen, T. Advances in 3D Printing Materials Processing-Environmental Impacts and Alleviation Measures. *Adv. Mater. Process. Technol.* **2022**, *8*, 1275–1285. [CrossRef]
67. Mao, M.; He, J.; Li, X.; Zhang, B.; Lei, Q.; Liu, Y.; Li, D. The Emerging Frontiers and Applications of High-Resolution 3D Printing. *Micromachines* **2017**, *8*, 113. [CrossRef]
68. Park, Y.-G.; Yun, I.; Chung, W.G.; Park, W.; Lee, D.H.; Park, J.-U. High-Resolution 3D Printing for Electronics. *Adv. Sci.* **2022**, *9*, 2104623. [CrossRef] [PubMed]
69. Ahn, D.; Stevens, L.M.; Zhou, K.; Page, Z.A. Rapid High-Resolution Visible Light 3D Printing. *ACS Cent. Sci.* **2020**, *6*, 1555–1563. [CrossRef]
70. Serra, T.; Planell, J.A.; Navarro, M. High-Resolution PLA-Based Composite Scaffolds via 3-D Printing Technology. *Acta Biomater.* **2013**, *9*, 5521–5530. [CrossRef]
71. Maurel, A.; Martinez, A.C.; Grugeon, S.; Panier, S.; Dupont, L.; Cortes, P.; Sherrard, C.G.; Small, I.; Sreenivasan, S.T.; Macdonald, E. Toward High Resolution 3D Printing of Shape-Conformable Batteries via Vat Photopolymerization: Review and Perspective. *IEEE Access* **2021**, *9*, 140654–140666. Available online: https://ieeexplore.ieee.org/abstract/document/9568946/ (accessed on 27 October 2023). [CrossRef]
72. Gao, X.; Zheng, M.; Yang, X.; Sun, R.; Zhang, J.; Sun, X. Emerging Application of 3D-Printing Techniques in Lithium Batteries: From Liquid to Solid. *Mater. Today* **2022**, *59*, 161–181. [CrossRef]
73. Zhou, S.; Usman, I.; Wang, Y.; Pan, A. 3D Printing for Rechargeable Lithium Metal Batteries. *Energy Storage Mater.* **2021**, *38*, 141–156. [CrossRef]
74. Mu, T.; Xiang, L.; Wan, X.; Lou, S.; Du, C.; Zuo, P.; Yin, G. Ultrahigh Areal Capacity Silicon Anodes Realized via Manipulating Electrode Structure. *Energy Storage Mater.* **2022**, *53*, 958–968. [CrossRef]
75. Zhang, M.; Mei, H.; Chang, P.; Cheng, L. 3D Printing of Structured Electrodes for Rechargeable Batteries. *J. Mater. Chem. A* **2020**, *8*, 10670–10694. [CrossRef]
76. Lyu, Z.; Lim, G.J.H.; Guo, R.; Kou, Z.; Wang, T.; Guan, C.; Ding, J.; Chen, W.; Wang, J. 3D-Printed MOF-Derived Hierarchically Porous Frameworks for Practical High-Energy Density Li–O_2 Batteries. *Adv. Funct. Mater.* **2019**, *29*, 1806658. [CrossRef]
77. Gao, X.; Yang, X.; Wang, S.; Sun, Q.; Zhao, C.; Li, X.; Liang, J.; Zheng, M.; Zhao, Y.; Wang, J.; et al. A 3D-Printed Ultra-High Se Loading Cathode for High Energy Density Quasi-Solid-State Li–Se Batteries. *J. Mater. Chem. A* **2020**, *8*, 278–286. [CrossRef]
78. Ma, J.; Zheng, S.; Zhou, F.; Zhu, Y.; Das, P.; Huang, R.; Zhang, L.; Wang, X.; Wang, H.; Cui, Y.; et al. All 3D Printing Lithium Metal Batteries with Hierarchically and Conductively Porous Skeleton for Ultrahigh Areal Energy Density. *Energy Storage Mater.* **2023**, *54*, 304–312. [CrossRef]
79. He, H.; Luo, D.; Zeng, L.; He, J.; Li, X.; Yu, H.; Zhang, C. 3D Printing of Fast Kinetics Reconciled Ultra-Thick Cathodes for High Areal Energy Density Aqueous Li–Zn Hybrid Battery. *Sci. Bull.* **2022**, *67*, 1253–1263. [CrossRef]
80. Wang, J.; Sun, Q.; Gao, X.; Wang, C.; Li, W.; Holness, F.B.; Zheng, M.; Li, R.; Price, A.D.; Sun, X.; et al. Toward High Areal Energy and Power Density Electrode for Li-Ion Batteries via Optimized 3D Printing Approach. *ACS Appl. Mater. Interfaces* **2018**, *10*, 39794–39801. [CrossRef]
81. Marschewski, J.; Brenner, L.; Ebejer, N.; Ruch, P.; Michel, B.; Poulikakos, D. 3D-Printed Fluidic Networks for High-Power-Density Heat-Managing Miniaturized Redox Flow Batteries. *Energy Environ. Sci.* **2017**, *10*, 780–787. [CrossRef]
82. Li, J.; Du, Z.; Ruther, R.E.; An, S.J.; David, L.A.; Hays, K.; Wood, M.; Phillip, N.D.; Sheng, Y.; Mao, C.; et al. Toward Low-Cost, High-Energy Density, and High-Power Density Lithium-Ion Batteries. *JOM* **2017**, *69*, 1484–1496. [CrossRef]
83. Liu, P.; Sherman, E.; Jacobsen, A. Design and Fabrication of Multifunctional Structural Batteries. *J. Power Sources* **2009**, *189*, 646–650. [CrossRef]
84. Park, Y.K.; Park, G.G.; Park, J.G.; Lee, J.W. Robust Free-Standing Electrodes for Flexible Lithium-Ion Batteries Prepared by a Conventional Electrode Fabrication Process. *Electrochim. Acta* **2017**, *247*, 371–380. [CrossRef]

85. Roberts, M.; Johns, P.; Owen, J.; Brandell, D.; Edstrom, K.; Enany, G.E.; Guery, C.; Golodnitsky, D.; Lacey, M.; Lecoeur, C.; et al. 3D Lithium Ion Batteries—From Fundamentals to Fabrication. *J. Mater. Chem.* **2011**, *21*, 9876–9890. [CrossRef]
86. Hao, F.; Han, F.; Liang, Y.; Wang, C.; Yao, Y. Architectural Design and Fabrication Approaches for Solid-State Batteries. *MRS Bull.* **2018**, *43*, 775–781. [CrossRef]
87. Bhosale, V.S.; Gaikwad, P.M.; Maladkar, N.P.; Desai, K.V. A Review on Use of 3D Printing for Battery Manufacturing. *JETIR* **2022**, *9*, 21–28.
88. Divakaran, N.; Das, J.P.; PV, A.K.; Mohanty, S.; Ramadoss, A.; Nayak, S.K. Comprehensive Review on Various Additive Manufacturing Techniques and Its Implementation in Electronic Devices. *J. Manuf. Syst.* **2022**, *62*, 477–502. [CrossRef]
89. Bates, A.M.; Preger, Y.; Torres-Castro, L.; Harrison, K.L.; Harris, S.J.; Hewson, J. Are Solid-State Batteries Safer than Lithium-Ion Batteries? *Joule* **2022**, *6*, 742–755. [CrossRef]
90. He, Y.; Chen, S.; Nie, L.; Sun, Z.; Wu, X.; Liu, W. Stereolithography Three-Dimensional Printing Solid Polymer Electrolytes for All-Solid-State Lithium Metal Batteries. *Nano Lett.* **2020**, *20*, 7136–7143. [CrossRef]
91. Zekoll, S.; Marriner-Edwards, C.; Hekselman, A.K.O.; Kasemchainan, J.; Kuss, C.; Armstrong, D.E.J.; Cai, D.; Wallace, R.J.; Richter, F.H.; Thijssen, J.H.J.; et al. Hybrid Electrolytes with 3D Bicontinuous Ordered Ceramic and Polymer Microchannels for All-Solid-State Batteries. *Energy Environ. Sci.* **2018**, *11*, 185–201. [CrossRef]
92. Zaman, W.; Hatzell, K.B. Processing and Manufacturing of next Generation Lithium-Based All Solid-State Batteries. *Curr. Opin. Solid State Mater. Sci.* **2022**, *26*, 101003. [CrossRef]
93. Schnell, J.; Tietz, F.; Singer, C.; Hofer, A.; Billot, N.; Reinhart, G. Prospects of Production Technologies and Manufacturing Costs of Oxide-Based All-Solid-State Lithium Batteries. *Energy Environ. Sci.* **2019**, *12*, 1818–1833. [CrossRef]
94. Rogers, J.A.; DeSimone, J.M. Novel Materials. *Proc. Natl. Acad. Sci. USA* **2016**, *113*, 11667–11669. [CrossRef] [PubMed]
95. Ding, L.; Jiang, M.; Li, J.; Wen, J.; Zeng, M. Kill Two Birds with One Stone: MOFs with Carboxyl Functionalized Channels Are Used in Lithium Battery Negative Terminals and Zinc-Ion Batteries. *J. Energy Storage* **2024**, *85*, 111169. [CrossRef]
96. Budinoff, H.D.; McMains, S. Will It Print: A Manufacturability Toolbox for 3D Printing. *Int. J. Interact. Des. Manuf.* **2021**, *15*, 613–630. [CrossRef]
97. Li, H.; Liang, J. Recent Development of Printed Micro-Supercapacitors: Printable Materials, Printing Technologies, and Perspectives. *Adv. Mater.* **2020**, *32*, 1805864. [CrossRef] [PubMed]
98. Lin, Y.; Gao, Y.; Fang, F.; Fan, Z. Recent Progress on Printable Power Supply Devices and Systems with Nanomaterials. *Nano Res.* **2018**, *11*, 3065–3087. [CrossRef]
99. Ma, J.; Zheng, S.; Chi, L.; Liu, Y.; Zhang, Y.; Wang, K.; Wu, Z.-S. 3D Printing Flexible Sodium-Ion Microbatteries with Ultrahigh Areal Capacity and Robust Rate Capability. *Adv. Mater.* **2022**, *34*, 2205569. [CrossRef]
100. Nofal, M.; Al-Hallaj, S.; Pan, Y. Thermal Management of Lithium-Ion Battery Cells Using 3D Printed Phase Change Composites. *Appl. Therm. Eng.* **2020**, *171*, 115126. [CrossRef]
101. Liu, Y.; Qiao, Y.; Zhang, Y.; Yang, Z.; Gao, T.; Kirsch, D.; Liu, B.; Song, J.; Yang, B.; Hu, L. 3D Printed Separator for the Thermal Management of High-Performance Li Metal Anodes. *Energy Storage Mater.* **2018**, *12*, 197–203. [CrossRef]
102. Lewis, J.A. Direct Ink Writing of 3D Functional Materials. *Adv. Funct. Mater.* **2006**, *16*, 2193–2204. [CrossRef]
103. Tagliaferri, S.; Panagiotopoulos, A.; Mattevi, C. Direct Ink Writing of Energy Materials. *Mater. Adv.* **2021**, *2*, 540–563. [CrossRef]
104. Saadi, M.A.S.R.; Maguire, A.; Pottackal, N.T.; Thakur, M.S.H.; Ikram, M.M.; Hart, A.J.; Ajayan, P.M.; Rahman, M.M. Direct Ink Writing: A 3D Printing Technology for Diverse Materials. *Adv. Mater.* **2022**, *34*, 2108855. [CrossRef] [PubMed]
105. Guo, Z.; Yu, P.; Liu, Y.; Zhao, J. High-Precision Resistance Strain Sensors of Multilayer Composite Structure via Direct Ink Writing: Optimized Layer Flatness and Interfacial Strength. *Compos. Sci. Technol.* **2021**, *201*, 108530. [CrossRef]
106. Chen, B.; Willenbacher, N. High-Precision Direct Ink Writing of $Li_{6.4}La_3Zr_{1.4}Ta_{0.6}O_{12}$. *J. Eur. Ceram. Soc.* **2022**, *42*, 7491–7500. [CrossRef]
107. Loaldi, D.; Piccolo, L.; Brown, E.; Tosello, G.; Shemelya, C.; Masato, D. Hybrid Process Chain for the Integration of Direct Ink Writing and Polymer Injection Molding. *Micromachines* **2020**, *11*, 509. [CrossRef] [PubMed]
108. Yuk, H.; Zhao, X. A New 3D Printing Strategy by Harnessing Deformation, Instability, and Fracture of Viscoelastic Inks. *Adv. Mater.* **2017**, *30*, 1704028. [CrossRef] [PubMed]
109. Rocha, V.G.; Saiz, E.; Tirichenko, I.S.; García-Tuñón, E. Direct Ink Writing Advances in Multi-Material Structures for a Sustainable Future. *J. Mater. Chem. A* **2020**, *8*, 15646–15657. [CrossRef]
110. Yirmibesoglu, O.D.; Simonsen, L.E.; Manson, R.; Davidson, J.; Healy, K.; Menguc, Y.; Wallin, T. Multi-Material Direct Ink Writing of Photocurable Elastomeric Foams. *Commun. Mater.* **2021**, *2*, 82. [CrossRef]
111. Xu, C.; Quinn, B.; Lebel, L.L.; Therriault, D.; L'Espérance, G. Multi-Material Direct Ink Writing (DIW) for Complex 3D Metallic Structures with Removable Supports. *ACS Appl. Mater. Interfaces* **2019**, *11*, 8499–8506. [CrossRef]
112. Renteria, A.; Balcorta, V.H.; Marquez, C.; Rodriguez, A.A.; Renteria-Marquez, I.; Regis, J.; Wilburn, B.; Patterson, S.; Espalin, D.; Tseng, T.-L.; et al. Direct Ink Write Multi-Material Printing of PDMS-BTO Composites with MWCNT Electrodes for Flexible Force Sensors. *Flex. Print. Electron.* **2022**, *7*, 015001. [CrossRef]
113. Cadiou, T.; Demoly, F.; Gomes, S. A Hybrid Additive Manufacturing Platform Based on Fused Filament Fabrication and Direct Ink Writing Techniques for Multi-Material 3D Printing. *Int. J. Adv. Manuf. Technol.* **2021**, *114*, 3551–3562. [CrossRef]
114. Mantelli, A.; Romani, A.; Suriano, R.; Levi, M.; Turri, S. Direct Ink Writing of Recycled Composites with Complex Shapes: Process Parameters and Ink Optimization. *Adv. Eng. Mater.* **2021**, *23*, 2100116. [CrossRef]

115. Wei, M.; Zhang, F.; Wang, W.; Alexandridis, P.; Zhou, C.; Wu, G. 3D Direct Writing Fabrication of Electrodes for Electrochemical Storage Devices. *J. Power Sources* **2017**, *354*, 134–147. [CrossRef]
116. He, W.; Chen, C.; Jiang, J.; Chen, Z.; Liao, H.; Dou, H.; Zhang, X. 3D Printed Multilayer Graphite@SiO Structural Anode for High-Loading Lithium-Ion Battery. *Batter. Supercaps* **2022**, *5*, e202100258. [CrossRef]
117. Li, Q.; Dong, Q.; Wang, J.; Xue, Z.; Li, J.; Yu, M.; Zhang, T.; Wan, Y.; Sun, H. Direct Ink Writing (DIW) of Graphene Aerogel Composite Electrode for Vanadium Redox Flow Battery. *J. Power Sources* **2022**, *542*, 231810. [CrossRef]
118. Zhu, C.; Schorr, N.B.; Qi, Z.; Wygant, B.R.; Turney, D.E.; Yadav, G.G.; Worsley, M.A.; Duoss, E.B.; Banerjee, S.; Spoerke, E.D.; et al. Direct Ink Writing of 3D Zn Structures as High-Capacity Anodes for Rechargeable Alkaline Batteries. *Small Struct.* **2023**, *4*, 2200323. [CrossRef]
119. Liu, Z.; Tian, X.; Liu, M.; Duan, S.; Ren, Y.; Ma, H.; Tang, K.; Shi, J.; Hou, S.; Jin, H.; et al. Direct Ink Writing of $Li_{1.3}Al_{0.3}Ti_{1.7}(PO_4)_3$-Based Solid-State Electrolytes with Customized Shapes and Remarkable Electrochemical Behaviors. *Small* **2021**, *17*, 2002866. [CrossRef]
120. Tao, R.; Gu, Y.; Sharma, J.; Hong, K.; Li, J. A Conformal Heat-Drying Direct Ink Writing 3D Printing for High-Performance Lithium-Ion Batteries. *Mater. Today Chem.* **2023**, *32*, 101672. [CrossRef]
121. Li, L.; Tan, H.; Yuan, X.; Ma, H.; Ma, Z.; Zhao, Y.; Zhao, J.; Wang, X.; Chen, D.; Dong, Y. Direct Ink Writing Preparation of $LiFePO_4$/MWCNTs Electrodes with High-Areal Li-Ion Capacity. *Ceram. Int.* **2021**, *47*, 21161–21166. [CrossRef]
122. Rasul, M.G.; Cheng, M.; Jiang, Y.; Pan, Y.; Shahbazian-Yassar, R. Direct Ink Printing of PVdF Composite Polymer Electrolytes with Aligned BN Nanosheets for Lithium-Metal Batteries. *ACS Nanosci. Au* **2022**, *2*, 297–306. [CrossRef] [PubMed]
123. Liu, C.; Zhao, N.; Xu, K.; Li, Y.; Mwizerwa, J.P.; Shen, J.; Chen, Z. High-Performance $LiFePO_4$ and SiO@C/Graphite Interdigitated Full Lithium-Ion Battery Fabricated via Low Temperature Direct Write 3D Printing. *Mater. Today Energy* **2022**, *29*, 101098. [CrossRef]
124. Rocha, V.G.; García-Tuñón, E.; Botas, C.; Markoulidis, F.; Feilden, E.; D'Elia, E.; Ni, N.; Shaffer, M.; Saiz, E. Multimaterial 3D Printing of Graphene-Based Electrodes for Electrochemical Energy Storage Using Thermoresponsive Inks. *ACS Appl. Mater. Interfaces* **2017**, *9*, 37136–37145. [CrossRef] [PubMed]
125. FDM vs. FFF: Differences and Comparison. Available online: https://www.xometry.com/resources/3d-printing/fdm-vs-fff-3d-printing/ (accessed on 24 January 2024).
126. Jones, R.; Haufe, P.; Sells, E.; Iravani, P.; Olliver, V.; Palmer, C.; Bowyer, A. RepRap—The Replicating Rapid Prototyper. *Robotica* **2011**, *29*, 177–191. [CrossRef]
127. Sells, E.; Bailard, S.; Smith, Z.; Bowyer, A.; Olliver, V. RepRap: The Replicating Rapid Prototyper: Maximizing Customizability by Breeding the Means of Production. In *Handbook of Research in Mass Customization and Personalization*; World Scientific Publishing Company: Singapore, 2009; pp. 568–580. ISBN 978-981-4280-25-9.
128. Bowyer, A. 3D Printing and Humanity's First Imperfect Replicator. *3D Print. Addit. Manuf.* **2014**, *1*, 4–5. [CrossRef]
129. Reyes, C.; Somogyi, R.; Niu, S.; Cruz, M.A.; Yang, F.; Catenacci, M.J.; Rhodes, C.P.; Wiley, B.J. Three-Dimensional Printing of a Complete Lithium Ion Battery with Fused Filament Fabrication. *ACS Appl. Energy Mater.* **2018**, *1*, 5268–5279. [CrossRef]
130. Reyes, C.; Wiley, B.J. 3D Printing a Complete Lithium Ion Battery with Fused Filament Fabrication. Available online: https://www.researchgate.net/publication/327735139_3D_Printing_a_Complete_Lithium_Ion_Battery_with_Fused_Filament_Fabrication (accessed on 2 November 2023).
131. Mecheter, A.; Tarlochan, F. Fused Filament Fabrication Three-Dimensional Printing: Assessing the Influence of Geometric Complexity and Process Parameters on Energy and the Environment. *Sustainability* **2023**, *15*, 12319. [CrossRef]
132. Sola, A. Materials Requirements in Fused Filament Fabrication: A Framework for the Design of Next-Generation 3D Printable Thermoplastics and Composites. *Macromol. Mater. Eng.* **2022**, *307*, 2200197. [CrossRef]
133. Maurel, A.; Courty, M.; Fleutot, B.; Tortajada, H.; Prashantha, K.; Armand, M.; Grugeon, S.; Panier, S.; Dupont, L. Highly Loaded Graphite–Polylactic Acid Composite-Based Filaments for Lithium-Ion Battery Three-Dimensional Printing. *Chem. Mater.* **2018**, *30*, 7484–7493. [CrossRef]
134. Baechler, C.; DeVuono, M.; Pearce, J.M. Distributed Recycling of Waste Polymer into RepRap Feedstock. *Rapid Prototyp. J.* **2013**, *19*, 118–125. [CrossRef]
135. Cruz Sanchez, F.A.; Boudaoud, H.; Hoppe, S.; Camargo, M. Polymer Recycling in an Open-Source Additive Manufacturing Context: Mechanical Issues. *Addit. Manuf.* **2017**, *17*, 87–105. [CrossRef]
136. Cruz Sanchez, F.A.; Boudaoud, H.; Camargo, M.; Pearce, J.M. Plastic Recycling in Additive Manufacturing: A Systematic Literature Review and Opportunities for the Circular Economy. *J. Clean. Prod.* **2020**, *264*, 121602. [CrossRef]
137. Dertinger, S.C.; Gallup, N.; Tanikella, N.G.; Grasso, M.; Vahid, S.; Foot, P.J.S.; Pearce, J.M. Technical Pathways for Distributed Recycling of Polymer Composites for Distributed Manufacturing: Windshield Wiper Blades. *Resour. Conserv. Recycl.* **2020**, *157*, 104810. [CrossRef]
138. Redondo, E.; Pumera, M. Fully Metallic Copper 3D-Printed Electrodes via Sintering for Electrocatalytic Biosensing. *Appl. Mater. Today* **2021**, *25*, 101253. [CrossRef]
139. Mo, F.; Guo, B.; Liu, Q.; Ling, W.; Liang, G.; Chen, L.; Yu, S.; Wei, J. Additive Manufacturing for Advanced Rechargeable Lithium Batteries: A Mini Review. *Front. Energy Res.* **2022**, *10*, 986985. [CrossRef]
140. Chen, Y.; Liu, Y.; Chen, J.; Wang, Z.; Tang, B. Hybrid Energy Storage System Design for Mobile Multi-Material Fused Deposition Modeling. *AIP Adv.* **2020**, *10*, 075322. [CrossRef]

141. Anzalone, G.C.; Wijnen, B.; Pearce, J.M. Multi-Material Additive and Subtractive Prosumer Digital Fabrication with a Free and Open-Source Convertible Delta RepRap 3-D Printer. *Rapid Prototyp. J.* **2015**, *21*, 506–519. [CrossRef]
142. Sujithra, R.; Dhatreyi, B.; Saritha, D. Nanomaterials-Based Additive Manufacturing for Mass Production of Energy Storage Systems: 3D Printed Batteries and Supercapacitors. In *Nanotechnology-Based Additive Manufacturing: Product Design, Properties and Applications*; Wiley: New York, NY, USA, 2023.
143. Maurel, A. Thermoplastic Composite Filaments Formulation and 3D-Printing of a Lithium-Ion Battery via Fused Deposition Modeling. Ph.D. Thesis, Université de Picardie Jules Verne, Amiens, France, 2020.
144. Sanumi, O.J.; Ndungu, P.G.; Oboirien, B.O. Challenges of 3D Printing in LIB Electrodes: Emphasis on Material-Design Properties, and Performance of 3D Printed Si-Based LIB Electrodes. *J. Power Sources* **2022**, *543*, 231840. [CrossRef]
145. Laureto, J.J.; Pearce, J.M. Anisotropic Mechanical Property Variance between ASTM D638-14 Type i and Type Iv Fused Filament Fabricated Specimens. *Polym. Test.* **2018**, *68*, 294–301. [CrossRef]
146. Gao, X.; Qi, S.; Kuang, X.; Su, Y.; Li, J.; Wang, D. Fused Filament Fabrication of Polymer Materials: A Review of Interlayer Bond. *Addit. Manuf.* **2021**, *37*, 101658. [CrossRef]
147. Beydaghi, H.; Abouali, S.; Thorat, S.B.; Del Rio Castillo, A.E.; Bellani, S.; Lauciello, S.; Gentiluomo, S.; Pellegrini, V.; Bonaccorso, F. 3D Printed Silicon-Few Layer Graphene Anode for Advanced Li-Ion Batteries. *RSC Adv.* **2021**, *11*, 35051–35060. [CrossRef] [PubMed]
148. Maurel, A.; Grugeon, S.; Fleutot, B.; Courty, M.; Prashantha, K.; Tortajada, H.; Armand, M.; Panier, S.; Dupont, L. Three-Dimensional Printing of a $LiFePO_4$/Graphite Battery Cell via Fused Deposition Modeling. *Sci. Rep.* **2019**, *9*, 18031. [CrossRef] [PubMed]
149. Gao, W.; Michalička, J.; Pumera, M. Hierarchical Atomic Layer Deposited V_2O_5 on 3D Printed Nanocarbon Electrodes for High-Performance Aqueous Zinc-Ion Batteries. *Small* **2022**, *18*, 2105572. [CrossRef] [PubMed]
150. Foster, C.W.; Zou, G.; Jiang, Y.; Down, M.P.; Liauw, C.M.; Garcia-Miranda Ferrari, A.; Ji, X.; Smith, G.C.; Kelly, P.J.; Banks, C.E. Next-Generation Additive Manufacturing: Tailorable Graphene/Polylactic(Acid) Filaments Allow the Fabrication of 3D Printable Porous Anodes for Utilisation within Lithium-Ion Batteries. *Batter. Supercaps* **2019**, *2*, 448–453. [CrossRef]
151. Hu, X.; Chen, Y.; Xu, W.; Zhu, Y.; Kim, D.; Fan, Y.; Yu, B.; Chen, Y. 3D-Printed Thermoplastic Polyurethane Electrodes for Customizable, Flexible Lithium-Ion Batteries with an Ultra-Long Lifetime. *Small* **2023**, *19*, 2301604. [CrossRef] [PubMed]
152. Maurel, A.; Armand, M.; Grugeon, S.; Fleutot, B.; Davoisne, C.; Tortajada, H.; Courty, M.; Panier, S.; Dupont, L. Poly(Ethylene Oxide)−LiTFSI Solid Polymer Electrolyte Filaments for Fused Deposition Modeling Three-Dimensional Printing. *J. Electrochem. Soc.* **2020**, *167*, 070536. [CrossRef]
153. De Wolf, R.; De Rop, M.; Hereijgers, J. Effects of Structured 3D Electrodes on the Performance of Redox Flow Batteries. *ChemElectroChem* **2022**, *9*, e202200640. [CrossRef]
154. Yang, P.; Fan, H.J. Inkjet and Extrusion Printing for Electrochemical Energy Storage: A Minireview. *Adv. Mater. Technol.* **2020**, *5*, 2000217. [CrossRef]
155. Sousa, R.E.; Costa, C.M.; Lanceros-Méndez, S. Advances and Future Challenges in Printed Batteries. *ChemSusChem* **2015**, *8*, 3539–3555. [CrossRef]
156. Sztymela, K.; Bienia, M.; Rossignol, F.; Mailley, S.; Ziesche, S.; Varghese, J.; Cerbelaud, M. Fabrication of Modern Lithium Ion Batteries by 3D Inkjet Printing: Opportunities and Challenges. *Heliyon* **2022**, *8*, e12623. [CrossRef]
157. Sowade, E.; Polomoshnov, M.; Willert, A.; Baumann, R.R. Toward 3D-Printed Electronics: Inkjet-Printed Vertical Metal Wire Interconnects and Screen-Printed Batteries. *Adv. Eng. Mater.* **2019**, *21*, 1900568. [CrossRef]
158. Zhao, Y.; Zhou, Q.; Liu, L.; Xu, J.; Yan, M.; Jiang, Z. A Novel and Facile Route of Ink-Jet Printing to Thin Film SnO_2 Anode for Rechargeable Lithium Ion Batteries. *Electrochim. Acta* **2006**, *51*, 2639–2645. [CrossRef]
159. Lawes, S.; Sun, Q.; Lushington, A.; Xiao, B.; Liu, Y.; Sun, X. Inkjet-Printed Silicon as High Performance Anodes for Li-Ion Batteries. *Nano Energy* **2017**, *36*, 313–321. [CrossRef]
160. Chen, T.; Wang, Y.; Yang, Y.; Huang, F.; Zhu, M.; Ang, B.T.W.; Xue, J.M. Heterometallic Seed-Mediated Zinc Deposition on Inkjet Printed Silver Nanoparticles Toward Foldable and Heat-Resistant Zinc Batteries. *Adv. Funct. Mater.* **2021**, *31*, 2101607. [CrossRef]
161. Kushwaha, A.; Jangid, M.K.; Bhatt, B.B.; Mukhopadhyay, A.; Gupta, D. Inkjet-Printed Environmentally Friendly Graphene Film for Application as a High-Performance Anode in Li-Ion Batteries. *ACS Appl. Energy Mater.* **2021**, *4*, 7911–7921. [CrossRef]
162. Kushwaha, A.; Sharma, A.; Bhatt, B.B.; Mukhopadhyay, A.; Gupta, D. Inkjet-Printed Graphene-Modified Aluminum Current Collector for High-Voltage Lithium-Ion Battery. *ACS Appl. Energy Mater.* **2023**, *6*, 4168–4178. [CrossRef]
163. Viviani, P.; Gibertini, E.; Iervolino, F.; Levi, M.; Magagnin, L. Carbon Additive Effect on the Electrochemical Performances of Inkjet Printed Thin-Film $Li_4Ti_5O_{12}$ Electrodes. *J. Manuf. Process.* **2021**, *72*, 411–418. [CrossRef]
164. Kolchanov, D.S.; Mitrofanov, I.; Kim, A.; Koshtyal, Y.; Rumyantsev, A.; Sergeeva, E.; Vinogradov, A.; Popovich, A.; Maximov, M.Y. Inkjet Printing of Li-Rich Cathode Material for Thin-Film Lithium-Ion Microbatteries. *Energy Technol.* **2020**, *8*, 1901086. [CrossRef]
165. Pei, M.; Shi, H.; Yao, F.; Liang, S.; Xu, Z.; Pei, X.; Wang, S.; Hu, Y. 3D Printing of Advanced Lithium Batteries: A Designing Strategy of Electrode/Electrolyte Architectures. *J. Mater. Chem. A* **2021**, *9*, 25237–25257. [CrossRef]
166. Yang, Y.; Yuan, W.; Zhang, X.; Yuan, Y.; Wang, C.; Ye, Y.; Huang, Y.; Qiu, Z.; Tang, Y. Overview on the Applications of Three-Dimensional Printing for Rechargeable Lithium-Ion Batteries. *Appl. Energy* **2020**, *257*, 114002. [CrossRef]
167. Tian, X.; Zhou, K. 3D Printing of Cellular Materials for Advanced Electrochemical Energy Storage and Conversion. *Nanoscale* **2020**, *12*, 7416–7432. [CrossRef] [PubMed]

168. Narita, K.; Saccone, M.A.; Sun, Y.; Greer, J.R. Additive Manufacturing of 3D Batteries: A Perspective. *J. Mater. Res.* **2022**, *37*, 1535–1546. [CrossRef]
169. Mubarak, S.; Dhamodharan, D.; Byun, H.S. Recent Advances in 3D Printed Electrode Materials for Electrochemical Energy Storage Devices. *J. Energy Chem.* **2023**, *81*, 272–312. [CrossRef]
170. Cheng, M.; Deivanayagam, R.; Shahbazian-Yassar, R. 3D Printing of Electrochemical Energy Storage Devices: A Review of Printing Techniques and Electrode/Electrolyte Architectures. *Batter. Supercaps* **2020**, *3*, 130–146. [CrossRef]
171. Zakeri, S.; Vippola, M.; Levänen, E. A Comprehensive Review of the Photopolymerization of Ceramic Resins Used in Stereolithography. *Addit. Manuf.* **2020**, *35*, 101177. [CrossRef]
172. Brinckmann, S.A.; Patra, N.; Yao, J.; Ware, T.H.; Frick, C.P.; Fertig, R.S. Stereolithography of SiOC Polymer-Derived Ceramics Filled with SiC Micronwhiskers. *Adv. Eng. Mater.* **2018**, *20*, 1800593. [CrossRef]
173. Chen, Q.; Xu, R.; He, Z.; Zhao, K.; Pan, L. Printing 3D Gel Polymer Electrolyte in Lithium-Ion Microbattery Using Stereolithography. *J. Electrochem. Soc.* **2017**, *164*, A1852–A1857. [CrossRef]
174. Norjeli, M.F.; Tamchek, N.; Osman, Z.; Mohd Noor, I.S.; Kufian, M.Z.; Ghazali, M.I.B.M. Additive Manufacturing Polyurethane Acrylate via Stereolithography for 3D Structure Polymer Electrolyte Application. *Gels* **2022**, *8*, 589. [CrossRef]
175. Lee, K.; Shang, Y.; Bobrin, V.A.; Kuchel, R.; Kundu, D.; Corrigan, N.; Boyer, C. 3D Printing Nanostructured Solid Polymer Electrolytes with High Modulus and Conductivity. *Adv. Mater.* **2022**, *34*, 2204816. [CrossRef]
176. Katsuyama, Y.; Kudo, A.; Kobayashi, H.; Han, J.; Chen, M.; Honma, I.; Kaner, R.B. A 3D-Printed, Freestanding Carbon Lattice for Sodium Ion Batteries. *Small* **2022**, *18*, 2202277. [CrossRef]
177. Ye, X.; Wang, C.; Wang, L.; Lu, B.; Gao, F.; Shao, D. DLP Printing of a Flexible Micropattern Si/PEDOT:PSS/PEG Electrode for Lithium-Ion Batteries. *Chem. Commun.* **2022**, *58*, 7642–7645. [CrossRef] [PubMed]
178. Yoko, A.; Oshima, Y. Recovery of Silicon from Silicon Sludge Using Supercritical Water. *J. Supercrit. Fluids* **2013**, *75*, 1–5. [CrossRef]
179. Sun, L.; Liu, Y.; Wu, J.; Shao, R.; Jiang, R.; Tie, Z.; Jin, Z. A Review on Recent Advances for Boosting Initial Coulombic Efficiency of Silicon Anodic Lithium Ion Batteries. *Small* **2022**, *18*, 2102894. [CrossRef] [PubMed]
180. Pearce, J.M. Economic Savings for Scientific Free and Open Source Technology: A Review. *HardwareX* **2020**, *8*, e00139. [CrossRef] [PubMed]
181. Dobbelaere, T.; Vereecken, P.M.; Detavernier, C. A USB-Controlled Potentiostat/Galvanostat for Thin-Film Battery Characterization. *HardwareX* **2017**, *2*, 34–49. [CrossRef]
182. Sylvestrin, G.R.; Scherer, H.F.; Hideo Ando Junior, O. Hardware and Software Development of an Open Source Battery Management System. *IEEE Lat. Am. Trans.* **2021**, *19*, 1153–1163. [CrossRef]
183. Fleming, J.; Amietszajew, T.; McTurk, E.; Towers, D.P.; Greenwood, D.; Bhagat, R. Development and Evaluation of In-Situ Instrumentation for Cylindrical Li-Ion Cells Using Fibre Optic Sensors. *HardwareX* **2018**, *3*, 100–109. [CrossRef]
184. Carloni, A.; Baronti, F.; Di Rienzo, R.; Roncella, R.; Saletti, R. An Open-Hardware and Low-Cost Maintenance Tool for Light-Electric-Vehicle Batteries. *Energies* **2021**, *14*, 4962. [CrossRef]
185. Yensen, N.; Allen, P.B. Open Source All-Iron Battery for Renewable Energy Storage. *HardwareX* **2019**, *6*, e00072. [CrossRef]
186. Koirala, D.; Yensen, N.; Allen, P.B. Open Source All-Iron Battery 2.0. *HardwareX* **2021**, *9*, e00171. [CrossRef]
187. Liao, C. *Batteries: Materials Principles and Characterization Methods*; IOP Publishing: Bristol, UK, 2021; ISBN 978-0-7503-2682-7.
188. Reddy, T.B.; Linden, D. *Linden's Handbook of Batteries*, 4th ed.; McGraw-Hill Education: Berkshire, UK, 2011; ISBN 978-0-07-162421-3.
189. Battery University Homepage. Available online: https://batteryuniversity.com/ (accessed on 6 March 2024).
190. Kordesch, K.; Taucher-Mautner, W. *HISTORY | Primary Batteries*; Elsevier: Amsterdam, The Netherlands, 2009; pp. 555–564. [CrossRef]
191. Owens, B.B.; Reale, P.; Scrosati, B. *PRIMARY BATTERIES | Overview*; Elsevier: Amsterdam, The Netherlands, 2009; pp. 22–27. [CrossRef]
192. When to Use Rechargeable Batteries. Available online: https://www.consumerreports.org/electronics-computers/batteries/when-to-use-rechargeable-batteries-a1076298884/ (accessed on 14 January 2024).
193. Lopes, P.P.; Stamenkovic, V.R. Past, Present, and Future of Lead–Acid Batteries. *Science* **2020**, *369*, 923–924. [CrossRef] [PubMed]
194. The Role of Energy Storage in Low-Carbon Energy Systems. In *Storing Energy*; Elsevier: Amsterdam, The Netherlands, 2016; pp. 3–22.
195. Viswanathan, B. (Ed.) Chapter 12—Batteries. In *Energy Sources*; Elsevier: Amsterdam, The Netherlands, 2017; pp. 263–313. ISBN 978-0-444-56353-8.
196. Burheim, O.S. Secondary Batteries. In *Engineering Energy Storage*; Elsevier: Amsterdam, The Netherlands, 2017; pp. 111–145. ISBN 978-0-12-814100-7.
197. May, G.J.; Davidson, A.; Monahov, B. Lead Batteries for Utility Energy Storage: A Review. *J. Energy Storage* **2018**, *15*, 145–157. [CrossRef]
198. Doughty, D.H.; Roth, E.P. A General Discussion of Li Ion Battery Safety. *Electrochem. Soc. Interface* **2012**, *21*, 37. [CrossRef]
199. Flora, G.; Gupta, D.; Tiwari, A. Toxicity of Lead: A Review with Recent Updates. *Interdiscip. Toxicol.* **2012**, *5*, 47–58. [CrossRef] [PubMed]
200. Posada, J.O.G.; Rennie, A.J.R.; Villar, S.P.; Martins, V.L.; Marinaccio, J.; Barnes, A.; Glover, C.F.; Worsley, D.A.; Hall, P.J. Aqueous Batteries as Grid Scale Energy Storage Solutions. *Renew. Sustain. Energy Rev.* **2017**, *68*, 1174–1182. [CrossRef]

201. Quansah, D.A. Comparative Study of Electricity Storage Batteries for Solar Photovoltaic Home Systems. Ph.D. Dissertation, Kwame Nkrumah University of Science and Technology, Kumasi, Ghana, 2008.
202. Marin-Garcia, G.; Vazquez-Guzman, G.; Sosa, J.M.; Lopez, A.R.; Martinez-Rodriguez, P.R.; Langarica, D. Battery Types and Electrical Models: A Review. In Proceedings of the 2020 IEEE International Autumn Meeting on Power, Electronics and Computing (ROPEC), Ixtapa, Mexico, 4–6 November 2020; pp. 1–6.
203. Poullikkas, A. A Comparative Overview of Large-Scale Battery Systems for Electricity Storage. *Renew. Sustain. Energy Rev.* **2013**, *27*, 778–788. [CrossRef]
204. Ramachandra Rao, S. Resource Recovery from Process Wastes. In *Waste Management Series*; Elsevier: Amsterdam, The Netherlands, 2006; Volume 7, pp. 375–457. ISBN 978-0-08-045131-2.
205. Beaudin, M.; Zareipour, H.; Schellenberg, A.; Rosehart, W. Energy Storage for Mitigating the Variability of Renewable Electricity Sources. In *Energy Storage for Smart Grids*; Elsevier: Amsterdam, The Netherlands, 2015; pp. 1–33. ISBN 978-0-12-410491-4.
206. Avril, S.; Arnaud, G.; Florentin, A.; Vinard, M. Multi-Objective Optimization of Batteries and Hydrogen Storage Technologies for Remote Photovoltaic Systems. *Energy* **2010**, *35*, 5300–5308. [CrossRef]
207. Divya, K.C.; Østergaard, J. Battery Energy Storage Technology for Power Systems—An Overview. *Electr. Power Syst. Res.* **2009**, *79*, 511–520. [CrossRef]
208. Parker, C.D. APPLICATIONS—STATIONARY | Energy Storage Systems: Batteries. In *Encyclopedia of Electrochemical Power Sources*; Elsevier: Amsterdam, The Netherlands, 2009; pp. 53–64. ISBN 978-0-444-52745-5.
209. Lemaire-Potteau, E.; Perrin, M.; Genies, S. BATTERIES | Charging Methods. In *Encyclopedia of Electrochemical Power Sources*; Elsevier: Amsterdam, The Netherlands, 2009; pp. 413–423. ISBN 978-0-444-52745-5.
210. Zhu, W.H.; Zhu, Y.; Davis, Z.; Tatarchuk, B.J. Energy Efficiency and Capacity Retention of Ni–MH Batteries for Storage Applications. *Appl. Energy* **2013**, *106*, 307–313. [CrossRef]
211. Abdin, Z.; Khalilpour, K.R. Single and Polystorage Technologies for Renewable-Based Hybrid Energy Systems. In *Polygeneration with Polystorage for Chemical and Energy Hubs*; Elsevier: Amsterdam, The Netherlands, 2019; pp. 77–131. ISBN 978-0-12-813306-4.
212. Iclodean, C.; Varga, B.; Burnete, N.; Cimerdean, D.; Jurchiş, B. Comparison of Different Battery Types for Electric Vehicles. *IOP Conf. Ser. Mater. Sci. Eng.* **2017**, *252*, 012058. [CrossRef]
213. Bernard, P.; Lippert, M. Nickel–Cadmium and Nickel–Metal Hydride Battery Energy Storage. In *Electrochemical Energy Storage for Renewable Sources and Grid Balancing*; Elsevier: Amsterdam, The Netherlands, 2015; pp. 223–251. ISBN 978-0-444-62616-5.
214. German, J.M. Hybrid Electric Vehicles. In *Encyclopedia of Energy*; Elsevier: Amsterdam, The Netherlands, 2004; pp. 197–213. ISBN 978-0-12-176480-7.
215. Tsais, P.-J.; Chan, L.I. Nickel-Based Batteries: Materials and Chemistry. In *Electricity Transmission, Distribution and Storage Systems*; Elsevier: Amsterdam, The Netherlands, 2013; pp. 309–397. ISBN 978-1-84569-784-6.
216. Aktaş, A.; Kirçiçek, Y. Solar Hybrid Systems and Energy Storage Systems. In *Solar Hybrid Systems*; Elsevier: Amsterdam, The Netherlands, 2021; pp. 87–125. ISBN 978-0-323-88499-0.
217. Cao, C.; Steinrück, H.-G. Molecular-Scale Synchrotron X-ray Investigations of Solid-Liquid Interfaces in Lithium-Ion Batteries. In *Encyclopedia of Solid-Liquid Interfaces*; Elsevier: Amsterdam, The Netherlands, 2023; pp. 391–416. ISBN 978-0-323-85670-6.

Disclaimer/Publisher's Note: The statements, opinions and data contained in all publications are solely those of the individual author(s) and contributor(s) and not of MDPI and/or the editor(s). MDPI and/or the editor(s) disclaim responsibility for any injury to people or property resulting from any ideas, methods, instructions or products referred to in the content.